Preprints (www.preprints.org) | NOT PEER-REVIEWED | Posted: 24 May 2022 doi:10.20944/preprints202005.0233.v2

Supernova Plasma Effects on Extragalactic Light Fields

P. Marko
SXM Innovation Center
Correspondence: pmarko@siriusxm.com

Simulations based on Supernova (SN) observations predict several galactic SN explosions (SNe) occur every century. Unlike SNes within the Interstellar Medium (ISM) where ambient gas generally absorbs blast waves within a million years, SNes occurring in a rarified environment outside of the (ISM) generate blast waves which remain in a high velocity free expansion phase for more extended periods. The SN blast wave forms an expanding spherical shell and when multiple blast waves intersect, the overlapping region naturally takes the form of a ring, an arc, or an Einstein Cross structure. The analysis shows the high velocity plasma establishes a medium with permeability which drives the index of refraction greater than 1. As a result, when a shock discontinuity forms in the overlapping region, light is reflected from the host galaxy which exposes the intersecting blast wave regions. The expanding shells are shown to induce an achromatic redshift to the reflected light consistent with those measured for gravitational lenses. Further, it is shown that a Hubble equation for a blast wave around the Milky Way Galaxy can be parameterized to align with measured redshifts of extragalactic light fields over a wide range of distances.

Keywords: Supernova, Plasma, Gravitational Lens, Einstein Cross, Hubble Constant, Hubble Tension

1. Introduction

Ongoing technical advances in sensors, telescopes and light processing algorithms are enabling observations with higher image clarity, wider bandwidth and better spectrum resolution. These advances continue to expose additional details prompting the development of new or refined models and theories to better align with the data. In general, objects appearing in the light field have been accepted as being present at or near the observed position in space and any change to the light spectrum rest frequency is credited to Doppler shifts or inflation. As described here, when blast waves associated with SNes outside the ISM intersect, a shock interface, if formed, can induce reflections to EM waves in the form of rings, arcs or Einstein Cross structures. While plasmas are known to impact the propagation of electromagnetic (EM) waves associated with global navigation satellite systems at L-band, well known equations for the index of refraction predict plasmas become largely transparent as the frequency is increased [1]. High velocity plasmas are known to exhibit diamagnetism ($\mu_r < 1$) in static magnetic fields and when under the influence of the magnetic fields of incident EM waves [2]. While analysis of EM wave forces on high velocity plasmas shows particle forces are dominated by the electric field with resultant particle motion generating a magnetic field which increases permeability, the primary driver of permeability is the particle velocity imparted by the SNe, where during the period the electron crosses the path of an interacting photon soliton it introduces an asymmetric magnetic field within the interaction region which aligns in-phase with the photon magnetic field. When a medium with refractive index > 1 expands in the light path, a redshift is induced between stationary endpoints. As a result, host galaxy reflections from shock discontinuities formed by intersecting blast waves modeled with appropriate medium properties exhibit magnitudes and redshifts consistent with celestial observations. A Hubble equation derived for incoming light fields from extragalactic sources interacting with a singular blast wave is shown to induce an apparent recession velocity consistent with Hubble Constant measurement campaigns over a wide range of distances.

2. Supernova Blast Wave Model and Expansion Medium

Most of what is known and theorized about the SNe comes from photometric observations. The progenitors of SNes vary widely and can strongly influence the Circumstellar Medium (CSM) which

Preprints (www.preprints.org) | NOT PEER-REVIEWED | Posted: 24 May 2022 doi:10.20944/preprints202005.0233.v2

impacts the early phase of the blast wave. Type II SN progenitors may be massive hot stars expelling large amounts of mass in fast stellar winds. At the time the SN explodes it may be surrounded by a low density bubble encompassed in a thin dense shell formed by the wind interacting with the ISM. If the progenitor is a Red Supergiant (RSG) with a slower steady state wind when the star explodes, the profile of the density ρ will be $\rho \propto r^{-2}$. The progenitor may explode without evolving to a RSG or the RSG may contract prior to exploding creating more complex CSM and ISM interactions and structures [3-5].

Observations of Type Ia SNe affirm the explosions typically rise to maximum light in approximately 20 days, followed by a first rapid declining of about 3 orders of magnitude in approximately 30 days and then an exponential decay of one order of magnitude per month. Analysis of early phase spectra of Type Ia SN indicate the expanding ejecta is comprised of neutral and ionized intermediate-mass elements (O, Mg, Si, S, Ca) with some contribution from iron-peak elements (Fe, Ca) [6].

To a good approximation, the exploding material on the SN can be modeled as a fully ionized plasma [7]. Theoretical hydrodynamic explosion models for Type Ia SN have been developed based on observed light curves and spectra. While the models predict early phase ejecta velocities range from less than 100 km s^{-1} to over 25,000 km s^{-1}, multiple models predict a high density of ejecta material tightly grouped near 10,000 km s^{-1} [8].

Extensive research has been conducted on the evolution of the SNBW and for a SNe within the ISM the expanding ejecta is segmented into multiple phases as it interacts with the surrounding media [3,9]. This interaction begins in the Pre-Sedov-Taylor Phase which is characterized initially by free expansion where the SN ejecta moves radially outward at velocities in the range of 10^4 km s^{-1}. The ejecta leaves the star as a pressure pulse and transitions to a shock wave when it encounters gas in the CSM and ISM. The shock wave is characterized by a discontinuity in pressure which propagates through the gas and for simplicity can be modeled with a Friedlander waveform [10] described by

$$P(t) = P_s e^{\frac{-t}{t_a}}(1 - \frac{t}{t_a}) \qquad (1)$$

where $P(t)$ is the pressure versus time at a point in space, P_s is the overpressure and t_a is the time it takes for the overpressure to return to ambient pressure, as shown in Fig. 1 as a function of distance.

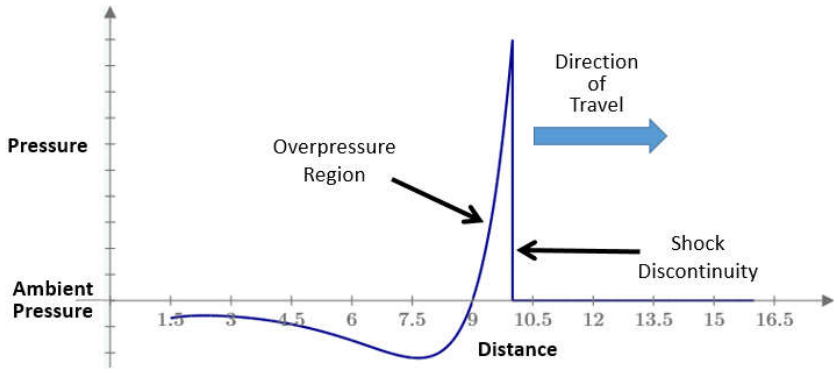

Fig. 1. SNBW pressure versus distance plot

Preprints (www.preprints.org) | NOT PEER-REVIEWED | Posted: 24 May 2022 doi:10.20944/preprints202005.0233.v2

Referring to Fig. 1, the shock discontinuity forms in ambient gas when the higher pressure portion of the pressure pulse catches up with the slower moving leading edge causing the leading edge to steepen. The behavior of the plasma across the discontinuity is defined by a set of jump conditions which constrain the fluid parameters and EM parameters to conserve mass, momentum and energy [11]. The width of the blast wave in Fig. 1 is defined here as the radial length the overpressure region remains above ambient pressure. As the blast wave expands with time, the width also expands due to variations in particle velocity and other factors discussed later.

Continuing in the Pre-Sedov-Taylor Phase, as the ejecta propagates into the ISM it shocks the gas and begins to sweep up interstellar material. The shock wave radius R expands with time t as $R \propto t$ during this phase and some ejecta kinetic energy is converted to heat. When the swept up mass is comparable to the initial mass of the ejecta approximately 70% of the initial energy has been converted to thermal energy and the shock wave enters the Sedov-Taylor Phase.

The Sedov-Taylor Phase is an energy conserving phase and the shock wave radius expands adiabatically with $\propto t^{\frac{2}{5}}$. Additional mass is swept up during this phase and the radial momentum increases. As the shock wave continues to expand, the temperature of the shock wave drops due to radiative cooling and a transition to the P. D. Snow Plow Phase begins. Radiative losses increase and as the shock front slows, higher velocity post-shock gas compresses behind the shock front to form a dense shell to begin the P. D. Snow Plow Phase. During the P. D. Snow Plow Phase, as the expanding dense shell continues to cool and sweep up interstellar material the shock velocity slows and the overall radial momentum drops. Finally, the Momentum-Conserving Snow Plow Phase begins once the shock front cools and the momentum of the shell is conserved. This phase eventually ends when the velocity of expansion slows to the sound speed of the ISM and the shock wave transitions to an acoustic wave. At this point the SN Remnant (SNR) has blended with the ISM and is no longer detectable. The time the SNBW remains in any of the phases is directly related to the characteristics of the surrounding ISM and in a non-homogeneous medium it is possible for some portions of the blast wave to simultaneously exist in different phases and at different distances from the blast center.

SNes provide an important feedback function to balance star formation in multiple models of disk galaxies [12-14]. SNe winds and outflows heat and redistribute material from the center of the galaxy to the outer regions and beyond and in galaxy models the process helps to reduce star formation to levels aligned with cosmic observations. The galactic winds driven by SNe also play a role in driving material into the Intergalactic Medium [15]. SNe-driven outflows can occur when multiple SNes are correlated in space and time such that the SNRs overlap and create superbubbles in the ISM [16,17]. These superbubbles can grow large enough to break out of the ISM disk and enable outflows of SNR material to escape into the CGM at velocities of up to several hundred km s^{-1} [18]. Another mechanism by which SNe-driven outflows can drive material into the IGM occurs if the SN explodes in a region of the galaxy where the ISM is very thin. In spiral galaxies, the ISM disk can extend above the galactic plane by 500 pc or more [19] before the density significantly drops. In observations of H II bubbles in galaxy M33, larger and more spherical bubbles have been detected with increasing galactocentric distance [20] indicative of the ISM thinning toward the outer edge of the ISM disk. Measurements of the ISM in elliptical galaxies show variations ranging from some galaxies having disturbed non-uniform ISMs [21] to others having ISMs which become increasingly thinner with galactocentric radius [22] to others with rare or missing ISMs [23,24]. Extragalactic statistics of SNe indicate elliptical galaxies have fewer SNe than spirals but the elliptical SNe rate per luminosity may be highest in halo stars which are generally in the outer thinner regions of the ISM [25].

Preprints (www.preprints.org) | NOT PEER-REVIEWED | Posted: 24 May 2022 doi:10.20944/preprints202005.0233.v2

The Kepler SNe is an example of a high above plane SN estimated to be at a distance ranging from 2.5 kpc to 12 kpc and a height above the galactic plane ranging from 380 pc to 1.4 kpc with more recent measurements favoring the lower end of the height range [26-28]. However, Kepler SN is not typical of an SNe in a rarified medium outside the ISM as Chandra observations show the Kepler ejecta spectra heavy with metallic ions indicating Kepler likely exploded in a dense CSM. The observations conflict with Kepler originating as a halo star or a runaway OB star or binary system as these are inconsistent with CSM abundancies [29], but the heavy CSM interaction and close proximity to the ISM are in alignment with the observed ejecta velocities.

In spiral galaxies, hydrodynamic simulations support the height of the SNe relative to the ISM is a major factor impacting the SNe-driven outflow [15]. When a SN explodes in the halo or in the CGM outside the ISM, referred to as a Circumgalactic SN (CG-SN) hereafter, as the shock wave leaves the CSM into the rarified CGM, the ejecta moving away from the galaxy encounters a CGM which is thinning with distance resulting in a shock wave which never sweeps up enough material to enter the Sedov-Taylor Phase. The ejecta moving toward the galaxy encounters the ISM and follows the SNBW evolution for SNes within the ISM. For the ejecta moving away from the galaxy, it is theorized the CG-SN blast wave energy converted to heat during the early phase rapidly cools as the blast wave expands at a velocity in the range of 10,000 km s^{-1}. The blast wave expanding into the rarified CGM is very difficult to detect as an ambient density of $>10^{-3}$ cm^{-3} is required to generate an observable radio emission [30].

CG-SNs are expected to comprise a very small percentage of the total SN occurrences. Based on extragalactic observations, models have been developed which estimate a total galactic SN rate of ~4.6 per century [31]. With the Circumgalactic Blast Wave (CG-BW) expanding at an average velocity of 0.025C, and with the Milky Way Galaxy at approximately 100k light years in diameter, a CG-SN explosion occurring above the ISM near the galactic center would take approximately 50k/0.025 = 2 million years to expand to the edge of the galaxy. If the SN rate of 4.6 per century is assumed constant during active SN epochs, approximately 92,000 SN explosions would have occurred during this period. Estimating substantially less than 1 in 1000 are either runaway OB stars or halo stars exploding as CG-SNs, less than 100 CG-BWs would be in a high velocity free expansion state traveling radially outward within a reference sphere encompassing the galaxy. As the SN rate changes over the evolution of the galaxy, in epochs of low SN activity the CGM may be void of CG-BWs in a free expansion state.

Observational evidence from Lyman Break Galaxies supports the CGM may be very thin near the galaxy as over millions of years SN-driven winds drive away intergalactic gas [32,33]. It has been estimated these outflows evacuating CGM material continue out to a galactopause at a range of 100-200 kpc where the outflows stall. The virial radius where this dynamic equilibrium happens in the Milky Way is estimated at 153 kpc [34] which is well beyond the CG-BW expansion ranges considered here. These estimates are supported by the COS-Halos Survey, where at these distances high metallicity ionized gas has been observed in the CGM of multiple low-redshift galaxies [35]. The galactic superwinds driving these outflows are difficult to observe and have implied wind fluid velocities of up to 3k km s^{-1} [36-38]. For the Milky Way, observations support the halo in the inner galaxy is comprised of irregular small and large scale structures of gas with large variations in temperature, density, composition and velocity [39,40]. Additional spectrographic studies of the Milky Way halo show many of the clouds consist of highly ionized high velocity gas, referred to as high velocity clouds (HVCs) [41]. As most HVC detection is based on line-of-sight absorption imprints on the relatively smooth continua of QSOs or low-redshift Type I Seyfert Galaxy nuclei, additional information is required to determine the distance to the HVCs, although it is generally accepted that much of the HVCs occur at large scale heights above the galactic plane. Observational constraints of many ionized HVCs lead to the conclusion that collisional

Preprints (www.preprints.org) | NOT PEER-REVIEWED | Posted: 24 May 2022 doi:10.20944/preprints202005.0233.v2

ionization is most probably the dominant ionization process [42]. Major theories for the origins of HVCs include 1) gas from the galactic disk being injected into the halo such as superbubble break outs and being further energized by stellar winds from young stars or SNes, 2) inflow of material from satellite galaxies such as the Magellanic Stream where some on the gas is tidally stripped and falls toward the galaxy disk and 3) dark matter-dominated gas clouds which flow along galactic filaments which fall toward the galaxy disk [43]. HVCs can be interpreted as evidence for the presence of CG-BWs in the halo as the high velocity ejecta can both collisionally ionize the clouds and drive the cloud kinetic energy [44]. These cloud interactions will create regions of low density or holes in the hemispherical surface of the free expanding CG-BW. In the Milky Way, halo observations show at galactocentric radii $R < 3$ kpc and a height above plane $z > 500$ pc there is virtually no gas detected which is consistent with the model that SN superwinds have driven out the gas over the range of 1-4 kpc [45]. For galactocentric radii R between 4 kpc and 8 kpc the halo between clouds becomes more quiescent with a density which drops exponentially with distance from the galactic plane.

Due to the low estimated rate of CG-SNs, the relatively short time window for detection before the ejecta becomes optically thin and the limitations in observations of the ISM and gaseous halo, direct evidence of a CG-BW is generally rare and subject to misinterpretation. A CG-SN with initial mass of 1 $M_{\odot}$ in free expansion may reach a radius of 200 LY within 10k years and with a shell thickness expansion rate 10% of the radial velocity, the ion particle density will already be below 10^{-4} cm^{-3} with a column density $<10^{15}$ cm^{-2}. The presence of multiple ion species in combination with a large velocity dispersion further reduces detectability by absorption spectroscopy. An absorption spectral imprint measured along a path normal to the wave surface with a uniform ion velocity dispersion of 1k km s^{-1} would be suppressed 20dB relative to an imprint of the same column density with a velocity dispersion equal to 10 km s^{-1}. An absorption measurement along a path tangent to the wave surface would not capture the true expansion and dispersion velocities and could be misinterpreted as an HVC cloud. Finding evidence of CG-SNs in gaseous halos is problematic as halos can be very extended with low surface brightness making them difficult to find. For example, a radio continuum survey of 181 nearby inclined galaxies showed only 7 with measurable emissions at high-z above the galactic plane [46]. For gaseous halo observations, since it is difficult to separate emissions coming from the galaxy disk and halo, observations on inclined galaxies are preferred at a cost of limiting kinematic information on the halo gas. In face-on extragalactic observations of the ISM, Hα surveys can provide evidence of recent SNe activity in close proximity to the galactic plane, but information on the height above the plane is not available. For example, in a survey of M33, multiple H II spherical bubbles have been detected but without enough information to conclude any one of the imprints were from an above plane CG-SN [20]. Above the galactic plane, large shells and super shells have been observed which are hemispherical and exhibit mass and kinetic energies far greater than a single SN [47,48]. Some of these shell structures can be created by CG-SNs efficiently transferring energy to nearby dense gaseous clouds.

Within the Milky Way, if a CG-SN explodes near the galactic bulge at a Circumgalactic distance less < 3 kpc and a height $z > 1$ kpc where there is virtually no gas, as the blast wave expands in the CGM largely unimpeded, the leading edge pressure discontinuity gradually softens and transitions back to a pressure pulse which diminishes any observable EM wave reflections associated with the difference between the refractive index of the blast wave plasma and the ambient media. In this case the reflection from the blast wave is analogous to a reflection in transmission line, where if an impedance discontinuity occurs along the transmission path some energy will be reflected and some transmitted in close approximation with the reflection coefficient

$$\Gamma = \frac{Z_2 - Z_1}{Z_2 + Z_1}. \qquad (2)$$

Preprints (www.preprints.org) | NOT PEER-REVIEWED | Posted: 24 May 2022 doi:10.20944/preprints202005.0233.v2

This equation is applicable to the blast wave where the incident EM wave travels from a media with characteristic impedance $Z_1$to a media with characteristic impedance Z_2 with the sign of the result describing the phase of the reflected electric field.

Tapering the transmission line at the interface to introduce a more gradual impedance transition is a common technique used to reduce reflections and minimize transmission losses [49]. In a blast wave propagating with a continuous tapered pressure profile, with the exception of refractive bending it can be shown EM waves will pass transparently through the wave including the condition where the plasma refractive index substantially differs from free space.

3. Overlapping CG-BW Structures as Gravitational Lenses

Gravitational lenses are widely observed in the universe and are theoretically formed when light from a distant galaxy passes near to a massive object, such as a foreground galaxy, where the associated gravitational pull bends the path of the light which commonly appears as an arc of light around the object. To further consider how free expanding CG-BWs can appear as a gravitational lens, it is appropriate to first review the plasma properties and environmental conditions impacting the refractive index.

Consider the case of two free expanding CG-BWs originating from two largely separated points in a galaxy, as depicted in Fig. 2a. The angle between the overlapping velocity vectors establishes the magnitude of the differential velocity vector which plays a key role in determining whether or not a shock discontinuity will form. At low acute angles the delta in velocity may not exceed the Alfven and sound speeds of the plasma and a shock condition may not be present. For higher acute angles, whether or not the shock conditions are met, the overlapping region can exhibit more complex behavior such as time dependent rotations of the planes of the magnetic fields and while the nature of such shocks is not fully understood [50], the shock discontinuity, if formed in the overlapping region, can be modeled as surfaces at the leading edge of each CG-BW.

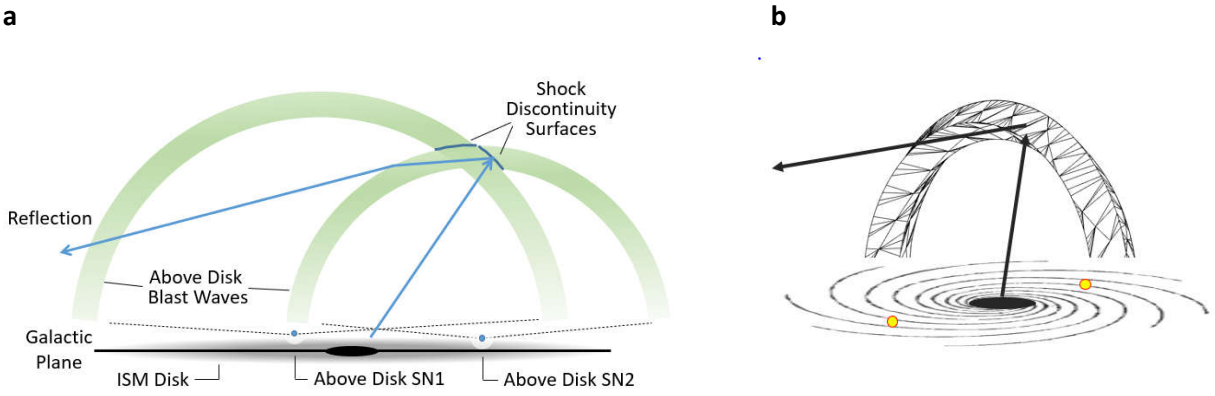

Fig. 2. Intersection of CG-SN Blast Waves. (**a**) Blast waves shown in green from SN1 and SN2 positioned apart in the galaxy intersect and form shock surfaces. Light from the galaxy can reflect off the shock discontinuity in the intersecting region. (**b**) Perspective view of the intersecting blast waves appearing as a partial ring.

The shock surfaces from the overlapping CG-BWs shown in Fig. 2a form a semicircle and reflect light from the host galaxy as shown in Fig. 2b and exposes the underlying structure. Since the reflecting surfaces are slices from a CG-BW hemisphere, the focal point for an extragalactic distant observer is approximately $1/2$ the CG-BW hemisphere radius towards the center and moves as the circular reflective surface is traversed. An extended arc of reflected light is effectively sourced from different portions of the host galaxy and can highlight the brightness patterns in an underlying spiral pattern. While the plasma

Preprints (www.preprints.org) | NOT PEER-REVIEWED | Posted: 24 May 2022 doi:10.20944/preprints202005.0233.v2

density on the shock surface is low, each photon reflected from the host galaxy is represented by a wave which is spread out over many square parsecs, increasing the effective number of particles associated with the reflection.

The light spectrum measured from these ring structures exhibit an additional redshift with respect to light from the host galaxy [51,52], implying the overlapping CG-BWs introduce a redshift. How this redshift occurs is described by first focusing on a single CG-BW. Assume the CG-BW were to expand from an initial width of 0.6 light days, based on 20 days of ejecta traveling at 0.025C after CSM interaction, to a width of 5k light years over a 2 million year period due to differences in initial particle velocity, changes in particle velocity induced by swept up matter and radial dispersion. If linear expansion is assumed for the width, the expansion rate is approximately 0.0025 light years per year which equates to a velocity $v_w = 750$ km s^{-1}. Although not included here, particle interaction in overlapping region is also expected to significantly contribute to the expansion velocity downstream of the leading edge.

The expanding width of a CG-BW induces a redshift in a manner analogous to a wedge moving through the light path as shown in Fig. 3. In Fig. 3a, initially an observer and remote light source are stationary in a medium with refractive index $\eta_0 = 1$ and no Doppler or redshift is present in the light received from the remote source.

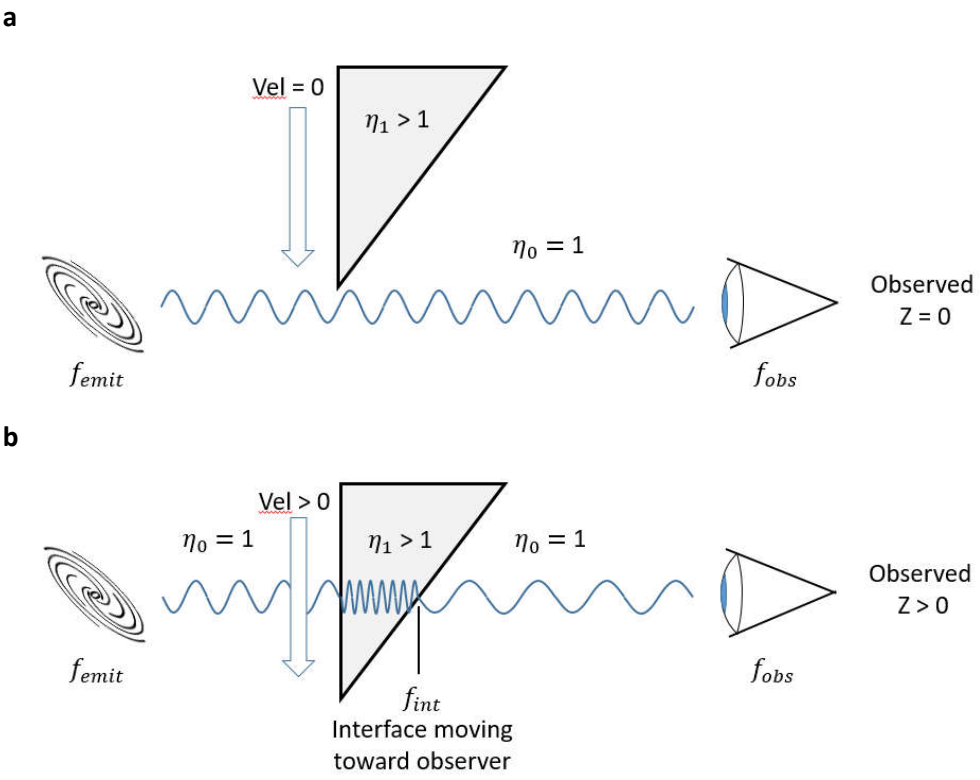

Fig. 3. Redshift *z* induced between stationary end points during refractive index change. (a) Steady state refractive index along the light path with no observed redshift. **(b)** Refractive index of the propagation path is increasing as the wedge ($\eta_1 > 1$) is expanding along the line of sight. With the wedge moving as shown the redshift present at the wedge interface receding from the emitter exceeds the blueshift from the wedge interface approaching the observer resulting in a net redshift along the observation path.

Preprints (www.preprints.org) | NOT PEER-REVIEWED | Posted: 24 May 2022 doi:10.20944/preprints202005.0233.v2

The wedge in Fig. 3b with refractive index $\eta_1 > 1$ is then moved perpendicular to the light path as shown with velocity v in m s^{-1} for a period T. During T, the wedge is displacing media with refractive index $\eta_0 = 1$ in the observation path with media with refractive index $\eta_1 > 1$. The velocity v_w at which the dielectric wedge width is growing along the observation path is

$$v_w = v * TAN\ \alpha \tag{3}$$

where α is the angle of the wedge leading edge. The net shift in the emission frequency f_{emit} can be determined by first calculating the frequency at the interface exiting the wedge f_{int} as it expands along the observation path. The frequency f_{int} with respect to f_{emit} is given by

$$f_{int} = \left(\frac{c/\eta_1 - v_w}{c/\eta_1}\right) f_{emit} \tag{4}$$

where c/η_1 is the speed of light in the wedge. Note for positive v_w the frequency is redshifted as the interface is receding from the source frequency at the wedge input. The frequency observed f_{obs} with respect to f_{int} is given by

$$f_{obs} = \left(\frac{c/\eta_0}{c/\eta_0 - v_w}\right) f_{int} \tag{5}$$

where c/η_0 is the speed of light in free space. For positive v_w the frequency observed is blueshifted as the wedge interface is moving toward the observer. Substituting for f_{int} and simplifying provides the relationship between f_{obs} and f_{emit} as

$$f_{obs} = \left(\frac{c - v_w\eta_1}{c - v_w\eta_0}\right) f_{emit.} \tag{6}$$

Based on this equation, when $v_w > 0$ and $\eta_1 > \eta_0$ a net redshift will be present along the observation path. When the wedge stops moving with $v_w = 0$ the redshift returns to zero. Moving the wedge laterally along the observation path does not store additional cycles in this example as the distance light travels through the wedge does not change. Note that it is possible to set η_1 such that $f_{obs} < 0$. In this case the wedge expansion velocity v_w is greater than the speed of light $^{c}/_{\eta_1}$ in the wedge, in which case light does not exit the wedge. Under these conditions f_{obs} = 0.

To further analyze the overlapping CG-BW case, consider a hypothetical example where a host galaxy is observed with a redshift $z = 3$ and the reflection from an overlapping CG-BW is observed with a redshift $z = 3.1$ which implies the reflected light has been redshifted by $z = 0.1$ relative to the host galaxy. The redshift z is defined as

$$z = \frac{f_{emit} - f_{obs}}{f_{obs}} \tag{7}$$

where f_{emit} is the source frequency, such as the Hα line at a rest frequency of 4.57 x 10^{14} Hz, and f_{obs} is the observed frequency. Solving equations (6) and (7) for η_1 with $\eta_0 = 1$ yields

$$\eta_1 = \frac{c(z+1) - (c - v_w)}{v_w(z+1)}. \tag{8}$$

Substituting $z = 0.1$, $v_w =$ 750 km s^{-1} and c = 3 x 10^8 m s^{-1} into equation (8) results a plasma refractive index $\eta_1 = 37$ which implies a relative permeability in the range of 1,369. The analysis in a later section will demonstrate higher values of v_w can drive up the redshift z with a much lower plasma refractive index.

Preprints (www.preprints.org) | NOT PEER-REVIEWED | Posted: 24 May 2022 doi:10.20944/preprints202005.0233.v2

4. Plasma Refractive Index

The refractive index η for EM radiation can be expressed

$$\eta = \sqrt{\epsilon_r \mu_r} \tag{9}$$

where ϵ_r is the media's relative permittivity and μ_r is the media's relative permeability. High velocity plasmas are known to exhibit diamagnetism ($\mu_r < 1$) when exposed to a static external magnetic field [2] where the Lorentz force drives the moving charged particles into a circular motion constituting a current loop with magnetic flux in opposition to the applied field. When high velocity plasmas are exposed to EM radiation, the charged particles are exposed to electromagnetic forces which drive particle motion. The EM wave consists of an electric field vector $\boldsymbol{E}$ and a magnetic field vector $\boldsymbol{B}$ which creates a force $\boldsymbol{F}$ on a moving particle of charge q according to the Lorentz equation

$$\boldsymbol{F} = q\boldsymbol{E} + q(\boldsymbol{v} \times \boldsymbol{B}) \tag{10}$$

where $q\boldsymbol{E}$ is the electric force, $q(\boldsymbol{v} \times \boldsymbol{B})$ is the magnetic force and $\boldsymbol{v}$ is the particle velocity vector. To determine the ratio of the electric force to the magnetic force, the characteristic impedance Z_p of the plasma [53] is determined based on the equation

$$Z_p = \sqrt{\frac{j\omega\mu_r\mu_0}{\sigma + j\omega\epsilon_r\epsilon_0}} \tag{11}$$

where σ is the plasma conductivity. For very low density plasmas the conductivity is near zero [54] which enables the simplification

$$Z_p = \sqrt{\frac{\mu_r\mu_0}{\epsilon_r\epsilon_0}} \tag{12}$$

where $\sqrt{\mu_0/\epsilon_0}$ is the intrinsic impedance of freespace Z_0. For an EM wave traveling in a media with characteristic impedance Z_p, the ratio of the electric field E to the magnetic field intensity H is set according to the equation

$$Z_p = \frac{E}{H} \tag{13}$$

and the implied the magnetic field flux density $B = \mu_r\mu_0 H$. While this magnetic flux density includes the cumulative contribution of the magnetic fields from charged particles in the medium through the factor μ_r and is applicable to the EM wave propagation properties, the individual charged particles are separated by relatively large distances and contributions from surrounding charges do not measurably enhance the magnetic flux density in the immediate vicinity of the particle. As a result, the magnetic field flux density driving the individual particle motion is $B = \mu_0 H$. Substitution yields

$$B = \mu_0 \frac{E}{Z_p} = \mu_0 \sqrt{\frac{\epsilon_r\epsilon_0}{\mu_r\mu_0}} E \tag{14}$$

and with the speed of light c_p in a plasma with relative permittivity ϵ_r and relative permeability μ_r defined as $c_p = 1/\sqrt{\epsilon_r\epsilon_0\mu_r\mu_0}$, this expression for magnetic flux density B can be reduced to

$$B = \frac{E}{\mu_r c_p} \tag{15}$$

Preprints (www.preprints.org) | NOT PEER-REVIEWED | Posted: 24 May 2022 doi:10.20944/preprints202005.0233.v2

where the terms are scaler values. By substitution, the amplitude of the magnetic force on a moving charged particle in the media can be expressed in terms of the electric field as

$$q\frac{v}{\mu_r c_p}E \tag{16}$$

and when $\mu_r = \epsilon_r = 1$, $c_p = \mathrm{C}$, the speed of light in vacuum, the magnitude of the magnetic force equals the electric force when the particle velocity v is equal to the speed of light C. With $\frac{v}{C} = 0.03$ for typical SN ejecta, the electric force dominates the opposing magnetic force and the resultant electric field-driven particle motion generates a magnetic field with paramagnetic properties. With the particle acceleration inversely proportional to the mass, the free electrons will experience a higher induced velocity and generate higher magnetic fields than the ions. To compute the expected magnitude of a reflection from overlapping SNBWs it is first necessary to determine the relative permeability of the medium established by the interaction of the EM wave with the thin plasma. As the particle density is low, the permeability is calculated based on the Effective Medium Theory, where the macroscopic electrodynamic properties of the medium are determined based on the microscopic fields associated with the charged particle interaction with the EM wave. The Effective Medium Theory for non-resonant particles can be expressed as

$$\mu_{eff} = A\mu_1 + (1 - A)\mu_0 \tag{17}$$

with

$$A = \frac{\pi D^2 b}{4a^2 H} \tag{18}$$

where μ_{eff} is the permeability of the composite medium, μ_1 is the permeability in the vicinity of the electron, μ_0 is the permeability of the medium between the electrons, the term $\pi D^2 b$ is the volume of a cylinder encompassing the photon-electron interaction area and the term $a^2 H$ is the average volume of free space surrounding the charged particle as defined by the inverse of the particle density [55]. The photon-electron interaction area approximates the photon soliton ellipsoid with a cylinder of radius $D = \frac{\lambda}{2\pi}$ and height $b = \lambda_{eff}$ [56], where $\lambda_{eff} = \frac{\lambda}{\eta_{eff}}$ and η_{eff} is the effective refractive index of the medium applicable to the direction of photon propagation.

Computation of the particle density in the SNBW assumes the mass of ejecta from each SNe is equal to 1 $M_\odot$. If the average atomic weight A_r of the ejecta ions is estimated at 16, the total number of ions N_i in each SNBW is given by

$$N_i = \frac{M_\odot \times N_A}{A_r} = 7.5 \times 10^{55} \tag{19}$$

where N_A is Avogadro's Number. Assuming the plasma is singly ionized, the total number of electrons N_e and ions are equal

$$N_e = N_i\ . \tag{20}$$

The volume occupied by the plasma is computed for two spherical shell sizes, a first estimated to extend from a radius of 45K Light Years (LY) to 50K LY and a second estimated to extend from a radius of 35K LY to 40K LY. The first shell occupies a volume Vol_{BW50} of 1.2 x 10^{62} m^3 and the second shell occupies a volume Vol_{BW40} of 7.5 x 10^{61} m^3. The electron density e_{dens} from the SNes in N_e m^{-3} is given by

$$e_{dens} = \frac{N_e}{Vol_{BW}}, \tag{21}$$

Preprints (www.preprints.org) | NOT PEER-REVIEWED | Posted: 24 May 2022 doi:10.20944/preprints202005.0233.v2

where for outer radius 50K LY $e_{dens50} = 6.2 \times 10^{-7}\ N_e$ m^{-3} and for outer radius 40K LY $e_{dens40} = 1.0 \times 10^{-6}\ N_e$ m^{-3} combining for a density of $e_{dens4050} = 1.62 \times 10^{-6}\ N_e$ m^{-3} where the shells overlap.

While equations 17-18 have been validated for a particle spacing less than a wavelength, it is noted that this limitation is in the context of laboratory measurements at microwave frequencies with the source close to the particles. When the spacing is converted particles per wavelength per source steradian, the particles per steradian scaled to cosmic distances effectively removes this limitation from the calculations here.

For the microscopic field calculations, the total composite average magnetic flux density B_t within the photon-matter interaction area when the photon passes a charged particle is defined as

$$B_t = \mu_r \mu_0 H_{pavg} = B_{lavg} + \mu_0 H_{pavg} \tag{22}$$

where μ_r is the relative permeability of the photon interaction with the charged particle. The term H_{pavg} is the average photon magnetic field intensity in A/m and B_{lavg} is the sum of the averaged non-photon magnetic flux densities correlated to the phase of the photon magnetic field, expressed as

$$B_{lavg} = B_{e\_i} + B_{gc} + B_{e\_bw} + B_{ap} \tag{23}$$

where B_{e_i} is the average electron flux density from the velocity induced by the composite galactic core field, B_{gc} is the average flux density from the galactic core, B_{e_bw} is the average electron flux density induced by blast wave velocity and B_{ap} is the summation of the average flux densities from adjacent particles which can be neglected in low density plasmas. Rearranging equation 22 and substituting $B_{pavg} = \mu_0 H_{pavg}$, μ_r in the photon interaction area can be expressed

$$\mu_r = \frac{B_{lavg}}{B_{pavg}} + 1 \tag{24}$$

where B_{lavg} and B_{pavg} are values averaged over a wavelength.

Preprints (www.preprints.org) | NOT PEER-REVIEWED | Posted: 24 May 2022 doi:10.20944/preprints202005.0233.v2

4.1 Electron Flux Density Induced by Photon

Considering an electron initially at rest, the electron magnetic field is shown with respect to the particle velocity induced by the EM wave in Fig 4a.

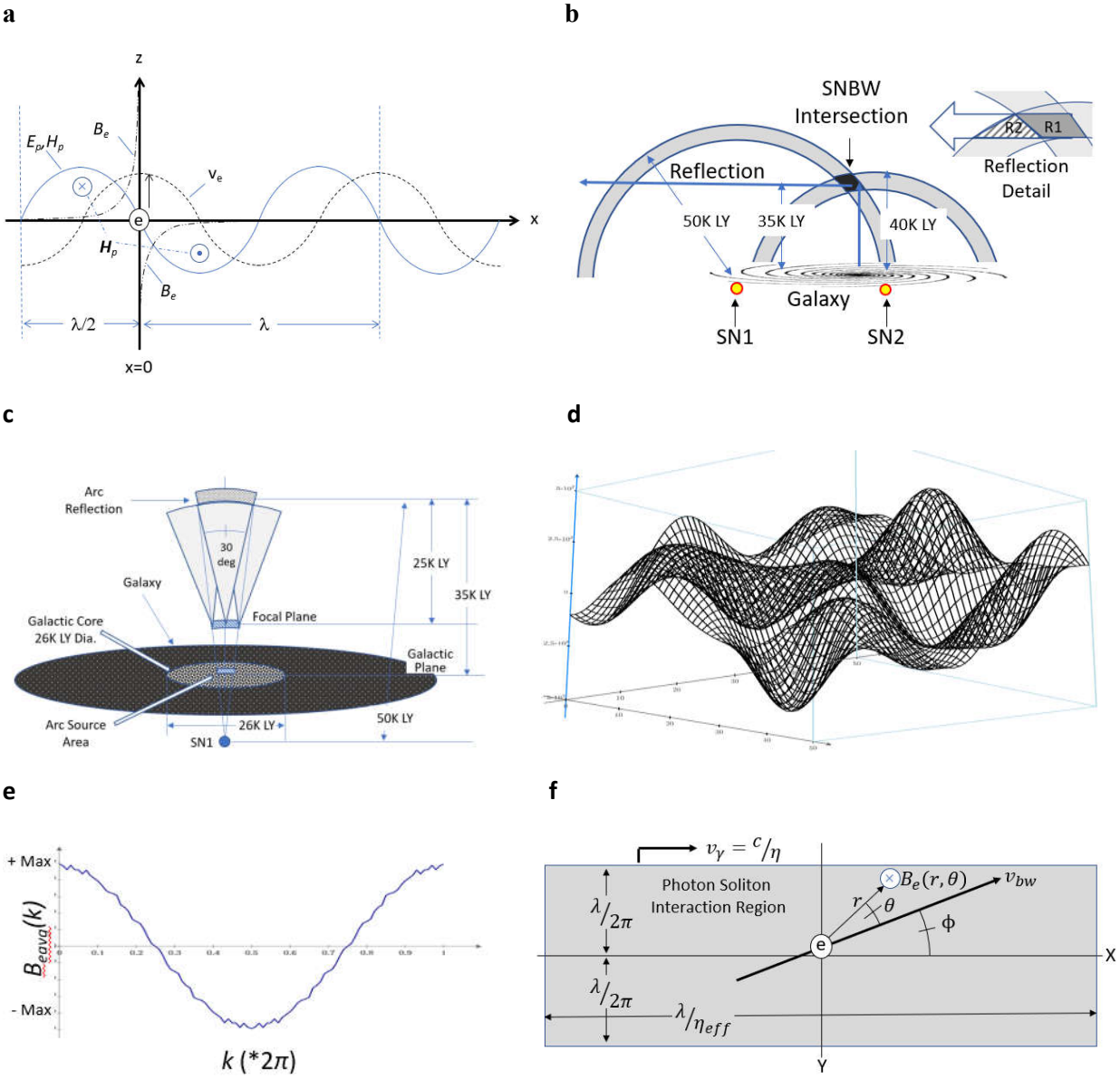

Fig. 4. SN Plasma Interaction with EM Wave. **(a)** EM wave (E_p, H_p) induces velocity v_e to electron e resulting in magnetic field B_e. **(b)** Overlapping SNBW diagram with plasma regions influencing reflection redshift shown. **(c)** Perspective diagram from direction of reflection showing overlapping arc segment above galaxy. **(d)** Typical instantaneous amplitude distribution of galaxy core light field in a 10λ x 10λ region. **(e)** Average electron magnetic flux density in phase with photon vs. phase of galaxy core field **(f)** Bounded photon soliton interaction region with high velocity electron magnetic field.

With reference to Fig. 4a, the EM wave of a photon stream traveling past the electron from left to right is shown by the E_p,H_p curve where the E-field vector along the z-axis and the H-field vector $\boldsymbol{H_p}$ is along the

Preprints (www.preprints.org) | NOT PEER-REVIEWED | Posted: 24 May 2022 doi:10.20944/preprints202005.0233.v2

y-axis which is orthogonal to the page. The electric force will induce the shown electron velocity v_e along the z-axis as a function of the EM wave phase along the x-axis given by

$$v_e(x) = v_{max}\cos(x) \tag{25}$$

where v_{max} is the maximum electron velocity which occurs when the EM field changes polarity. With $v \ll \mathrm{C}$, the EM wave-induced electron magnetic flux density at a point around the electron is given by

$$\boldsymbol{B_e}(r,\theta) \approx \frac{\mu_0}{4\pi}\frac{q}{r^2}(\boldsymbol{v_e} \times \hat{\boldsymbol{r}}) \tag{26}$$

where q is the charge, $\boldsymbol{v_e}$ is the electron velocity vector, r is the distance from the electron to the position of $\boldsymbol{B_e}$ and $\hat{\boldsymbol{r}}$ is the unit vector from the electron to $\boldsymbol{B_e}$. The induced magnetic flux density curve B_e shows the instantaneous amplitude normal to the induced velocity vector which decays with the square of the distance x from the electron with the direction of the B-field vector flipping from the left side of the electron to the right side. When the EM field changes polarity, the electron velocity and B-field are at a maximum and the B-field vectors align with the EM H-field vectors.

With the EM wave-induced magnetic flux density from the electron B_e having a magnitude profile which differs from the photon EM H-field, an average relative permeability is calculated by averaging the magnetic fields across a wavelength of the EM wave. The average photon EM field magnetic flux density is given by

$$B_{pavg} = \frac{2\mu_0}{\lambda_{eff}}\int_0^{\frac{\lambda_{eff}}{2}} H_{pmax}\sin\left(2\pi\frac{x}{\lambda_{eff}}\right)dx \tag{27}$$

where H_{pmax} is the peak magnetic field intensity per cycle. The instantaneous electron magnetic flux density averaged across a wavelength as a function of the instantaneous phase of the EM wave as it travels along the x-axis is given by

$$B_{einst}(x) = \frac{1}{\lambda_{eff}}\int_{\frac{\lambda_{eff}}{1000}}^{\frac{\lambda_{eff}}{2}}\left(\left(\frac{-\mu_0 q_e v_e(x)}{4\pi r^2}\psi(x+r)\right) + \left(\frac{\mu_0 q_e v_e(x)}{4\pi r^2}\psi(x-r)\right)\right)dr \tag{28}$$

where the first term in the integral is the flux left of the electron, the second term is the flux right of the electron, and the lower integration limit is set to avoid integrating across the electron core. The term $\psi(x)$ is the photon correlation function which assigns a sign to the flux density so that it adds or subtracts from the total flux as a function of the photon wave phase and removes any non-correlated components when integrated over a wavelength, with

$$\psi(x) = 1 \; if \; \sin\left(2\pi\frac{x}{\lambda_{eff}}\right) > 0 \tag{29}$$

$$= -1 \; if \; \sin\left(2\pi\frac{x}{\lambda_{eff}}\right) < 0$$

$$= 0 \; if \; \sin\left(2\pi\frac{x}{\lambda_{eff}}\right) = 0.$$

The instantaneous electron magnetic flux density averaged over a full wavelength of the passing photon wave is then given by

$$B_{eavg} = \frac{1}{\lambda_{eff}}\int_0^{\lambda_{eff}} B_{einst}(x)dx. \tag{30}$$

Preprints (www.preprints.org) | NOT PEER-REVIEWED | Posted: 24 May 2022 doi:10.20944/preprints202005.0233.v2

4.2 Electron Flux Density Induced by Galactic Core, B_{e_i}

Fig. 4b shows a simplified SNe arrangement for deriving the electrical properties of a reflection from the shock interface. The SNBW from SN1 has expanded to an outer radius of 50K LY and from SN2 to an outer radius of 40K LY and intersect at an approximate 75 degree angle 35K LY above the galactic core. Light from the galactic core reflects off the shock interface which appears as an arc to a distant observer.

Fig. 4c is a perspective view from the direction of the reflection. The analysis will initially focus on the reflection from a 30 degree arc sourced from the stars in the galactic core using typical Milky Way Galaxy parameters of core radius $R_{core} = 13K\ LY$ and core luminosity $L_{core} = 2.5 \times 10^{10}\ L_{\odot}$ [57]. As evident from Fig. 4c, the electrons within the arc will be primarily illuminated from the core stars, which for simplicity can be modeled with a total of 2.5×10^{10} stars, each with luminosity $L_{\odot}$, distributed over a $26K\ LY$ diameter disc spaced $35K\ LY$ away. The acceleration of the electrons within the overlap region will be primarily driven by the composite EM field radiated from the galactic core. If the energy were concentrated in a $H\alpha$ emission, an example of the instantaneous field strength spread over a 10λ x 10λ surface within the arc having Poynting vector normal to the disc is shown in Fig. 4d, which was generated using a uniform distribution of 10,000 randomly phased sources with geometry similar to Fig. 4c. With reference to Fig. 4a, when the electron is only influenced by the passing photon and the maximum electron velocity occurs as the photon magnetic field polarity flips, aligning the electron and photon magnetic fields to maximize the total magnetic field as described by equation 28. In Fig. 4c, the analysis will focus on the impact of the composite field from the galaxy core on the electron and the resultant magnetic field interactions with a coherent EM wave emanating from the core. Since photons simultaneously emitted from a star are sourced from points distributed over its surface, the composite field received at a distance of 35K LY does not exhibit coherence and is comprised of independent coherent EM waves from individual photon point sources. Accordingly, the coherent EM wave in the analysis is sourced from a coherent single photon point source and the derived properties are applicable to all individual photons forming the composite field. As the free electrons within the arc may be randomly located within the composite field when a photon wave from the core passes, the associated electron magnetic field will add to or subtract from the photon magnetic field based on the relative phase of the composite field. In Fig. 4a, the E_p,H_p curve from the photon source will be in a random alignment with the electron velocity v_e along the z-axis. For this case, equations 28 and 30 are modified to compute the instantaneous electron magnetic flux density averaged across a wavelength as a function of the instantaneous phase offset k of the photon as it travels along the x-axis as given by

$$B_{eavg}(k) = \frac{1}{{\lambda_{eff}}^2}\int_0^{\lambda_{eff}}\int_{\frac{\lambda_{eff}}{1000}}^{\frac{\lambda_{eff}}{2}}\left(\left(-\frac{\mu_0 q_e v_e(x)}{4\pi r^2}\psi(x+k+r)\right)+\left(\frac{\mu_0 q_e v_e(x)}{4\pi r^2}\psi(x+k-r)\right)\right)drdx. \quad (31)$$

Fig. 4e is a plot of B_{eavg} as a function of the phase k when the photon wave passes, where with a random phase there is an equal probability that a positive B_{eavg} will add to the photon magnetic field or negative B_{eavg} will subtract from the photon magnetic field. For negative B_{eavg}, if the relative permeability μ_r defined by equation 24 can become negative, and with the relative permittivity $\epsilon_r = 1$, the refractive index $\eta = \sqrt{\epsilon_r \mu_r}$ will be an imaginary value, where the photon will be subjected to attenuation or extinction α as a function of distance x in the B_{eavg} field according to

$$\alpha(x) = e^{-\frac{4\pi\eta x}{\lambda}} \quad (32)$$

and will not significantly contribute to the plasma permeability computed for the photon EM field propagating through the medium. From equation 21, the overlap region will have an electron density of

Preprints (www.preprints.org) | NOT PEER-REVIEWED | Posted: 24 May 2022 doi:10.20944/preprints202005.0233.v2

$1.62 \times 10^{-6}\ N_e$ m^{-3} and with approximately half inducing negative permeability, the column density of these electrons in the 5K LY overlap region will be $3.8 \times 10^{9}\ N_e$ cm^{-2}. As the observed extinction for neutral hydrogen has been characterized as

$$A(V)/N_H = 5.3 \times 10^{-22}\ \text{cm}^2 \tag{33}$$

where $A(V)$ is the total extinction in magnitudes and N_H is the hydrogen column density in cm^{-2} [58], if an electron with negative permeability has opacity within a few orders of magnitude of neutral hydrogen, it is evident the photon energy removed is small and can be neglected. The permeability is then computed using the half of the electrons that generate magnetic fields which add to the photon magnetic field. Continuing with Fig. 4c, the average intensity at the arc, I_{core}, from the galactic core 35K LY away can be approximated by

$$I_{core} = \frac{L_{core}}{4\pi \times (35 \times 10^3 \times LY)^2} = 6.98 \times 10^{-6}\ \text{W m}^{-2}. \tag{34}$$

The electric field within the arc from I_{core} is $E = \sqrt{Z \times I_{core}} = 5.1 \times 10^{-2}\ \text{V}_{\text{rms}}\ \text{m}^{-1} = 7.3 \times 10^{-2}\ \text{V}_{\text{pk}}\ \text{m}^{-1}$ which will introduce a maximum incremental velocity v_{emax} of 2.2×10^{-6} m s^{-1} parallel to the electric field vector and with phase relative to the composite field I_{core} as shown in Fig. 4a. With reference to the overlap region in Fig. 4b, the incremental velocity vector deviates from the initial electron velocity vector from SN1 and SN2 by approximately $\phi = 45$ and 60 degrees, respectively, and with the velocity in the range of 8,000 km s^{-1}, will have a negligible effect on the direction of the vectors.

As the electron will be randomly located within the composite field (Fig. 4d) and with the locations of the peak amplitude swings remaining relatively static over a single photon cycle, when the photon passes the maximum incremental velocity per cycle for electrons with B_{eavg} adding to the photon field would approach an average of

$$v_{e\_gcmax} = \frac{1}{\pi^2}\int_0^{\pi} sin^2\theta d\theta \times v_{emax} = 0.159 \times v_{emax}\ \text{m s}^{-1}. \tag{35}$$

Including the random phase of photon arrival where the electron magnetic field will add to the photon field, equation 31 can be revised to express the resultant B_{e_i} as

$$B_{e\_i} = \frac{1}{\lambda_{eff}^{\ 3}} \int_{-\frac{\lambda_{eff}}{2}}^{\frac{\lambda_{eff}}{2}} \int_0^{\lambda_{eff}} \int_{\frac{\lambda_{eff}}{1000}}^{\frac{\lambda_{eff}}{2}} \left(\left(-\frac{\mu_0 q_e v_{e\_gc}(x)\sin\phi}{4\pi r^2} \psi(x+k+r) \right) + \left(\frac{\mu_0 q_e v_{e\_gc}(x)\sin\phi}{4\pi r^2} \psi(x+k-r) \right) \right) dr dx dk \tag{36}$$

where $v_{e\_gc}(x) = v_{e\_gcmax}\cos(x)$.

4.3 Flux Density from Galactic Core, B_{gc}

Moving to the energy sourced from galactic core, the averaged magnetic flux density from the galaxy B_{gavg} is based on the composite intensity from the galaxy which is correlated in phase with the photon while it is interacting with the charged particle. For a photon in phase with the composite field, this is expressed by

$$B_{gavg} = \frac{1}{\lambda_{eff}} \int_0^{\lambda_{eff}} \mu_0 H_{gmax} \sin\left(2\pi \frac{x}{\lambda_{eff}}\right) \psi(x) dx \tag{37}$$

where H_{gmax} is the peak magnetic field intensity of the EM wave from the galaxy.

Preprints (www.preprints.org) | NOT PEER-REVIEWED | Posted: 24 May 2022 doi:10.20944/preprints202005.0233.v2

As discussed in Section 4.2, the free electrons which define the photon-matter interaction will be randomly located within the composite field when the photon wave passes. The averaging factor for the peak intensity defined in equation 35, $\frac{1}{\pi^2}\int_0^{\pi} sin^2\theta d\theta = 0.159$, is applicable and equation 31 is modified to compute the galactic core flux intensity averaged across a wavelength as a function of the instantaneous phase offset k of the photon with respect to the composite field as it travels along the x-axis to yield

$$B_{gavg}(k) = \frac{0.159}{\lambda_{eff}}\int_0^{\lambda_{eff}} \mu_0 H_{gmax} \sin\left(2\pi\frac{x}{\lambda_{eff}}\right)\psi(x+k)dx \qquad (38)$$

Assuming a uniform distribution of phase offsets across the photon wave as it interacts with electrons, the averaged magnetic flux density from the galactic core with a positive contribution to the photon magnetic field is

$$B_{gc} = \frac{1}{\lambda_{eff}}\int_{-\frac{\lambda_{eff}}{2}}^{\frac{\lambda_{eff}}{2}} B_{gavg}(k)dk. \qquad (39)$$

4.4 Electron Flux Density Induced by Blast Wave Velocity, B_{e_bw}

Next, the average flux density induced by the blast wave velocity B_{e_bw} is computed based on the diagram in Fig. 4f. With reference to Fig. 4f, the shaded region represents the photon soliton interaction region, which is modeled as a cylinder traveling from left to right with axis of symmetry along the x-axis which lies on a radial from the photon source (not shown). The electron travels with velocity v_{bw} with angle ϕ with respect to the photon velocity as shown. The magnetic field of the electron within the interaction region is evaluated only when the electron is within the interaction region. To compute the average electron magnetic flux density, the photon/electron interaction begins at time $t = 0$ with the photon traveling at velocity $c_{eff} = \frac{c}{\eta_{eff}}$ and the electron traveling at velocity v_{bw} with the photon interaction area positioned along the x-axis between $x = 0$ and $x = \lambda_{eff}$ and the electron positioned at $x = \lambda_{eff}, y = 0$ (not shown). The photon/electron interaction ends at time $t = \frac{\lambda_{eff}}{c_{eff} - v_{bw}\cos(\phi)}$ with the photon interaction area positioned between $x = \lambda_{eff}(1 + \frac{v_{bw}\cos(\phi)}{c_{eff} - v_{bw}\cos(\phi)})$ and $x = \lambda_{eff}(2 + \frac{v_{bw}\cos(\phi)}{c_{eff} - v_{bw}\cos(\phi)})$ which is where the photon/electron interaction area passes the electron (not shown). The average electron magnetic flux density as a function of time t and position x can be calculated by averaging along the y-axis as expressed by

$$B_{e\_bwy}(t,x) = \frac{\pi}{\lambda}\int_{-\frac{\lambda}{2\pi}}^{\frac{\lambda}{2\pi}} \frac{\mu_0 q_e v_{bw}}{4\pi((x')^2+(y')^2)} \sin(\text{atan}\left(\frac{y'}{x'}\right) - \phi)dy \qquad (40)$$

where $x' = x - (\lambda_{eff} + v_{bw}\cdot t\cdot cos(\phi))$, $y' = y - v_{bw}\cdot t\cdot \sin(\phi)$ and with constraints applied to insure the distance to the electron $(x')^2 + (y')^2$ does not drop below 10^{-14} m and $\sin(\text{atan}\left(\frac{y'}{x'}\right) - \phi)$ returns the correct angle in all 4 quadrants. The flux density at an instant in time can then be averaged over the photon while correcting for the phase of the photon magnetic field by

$$B_{e\_bwxy}(t) = \frac{1}{\lambda_{eff}}\int_{c_{eff}\cdot t}^{c_{eff}\cdot t+\lambda_{eff}} B_{e\_bwy}(t,x)\psi'(x - c_{eff}\cdot t)dx \qquad (41)$$

where

Preprints (www.preprints.org) | NOT PEER-REVIEWED | Posted: 24 May 2022 doi:10.20944/preprints202005.0233.v2

$$\psi'(x) = 0 \; if \; x < 0 \; or \; x > \lambda_{eff} \tag{42}$$
$$= -1 \; if \; \sin\left(2\pi \frac{x}{\lambda_{eff}}\right) > 0$$
$$= 1 \; if \; \sin\left(2\pi \frac{x}{\lambda_{eff}}\right) < 0$$
$$= 0 \; if \; \sin\left(2\pi \frac{x}{\lambda_{eff}}\right) = 0.$$

The electron magnetic flux density averaged over the period of photon/electron interaction is then given by

$$B_{e\_bw} = \frac{c_{eff} - v_{bw} \cdot \cos(\phi)}{\lambda_{eff}} \int_0^{\frac{\lambda_{eff}}{c_{eff} - v_{bw} \cdot \cos(\phi)}} B_{e\_bwxy}(t) dt. \tag{43}$$

Note that as the photon passes the electron, if the electron were to remain in a fixed position relative to the radial axis ($y = 0, \phi = 0$), the averaged electron magnetic flux density in the interaction region would be negligible. With $\phi \neq 0$, the electron moves across the photon radial axis as it passes and the asymmetry of the magnetic flux density versus time creates a significant average flux density as a function of the electron velocity and the angle ϕ.

With respect to equation 23, while the relevance of the various magnetic flux sources will vary by application, such as near-field microlensing refraction and overlapping BW reflections, it can be shown that with the high velocity from the SNe, B_{e_bw} dominates the average non-photon magnetic flux density. For the blast wave plasma, $B_{lavg} \cong B_{e\_bw}$ and equation 24 can be rewritten as

$$\mu_r = \frac{B_{e\_bw}}{B_{pavg}} + 1. \tag{44}$$

4.5 Plasma Permeability in Overlapping Region

With reference to Fig. 4b, since the electrons from SN1 and SN2 are crossing the photon path from the galactic center at different angles, B_{e_bw} is computed for each SN.

Substituting $\lambda = 6.57 \times 10^{-7}$ m, $\mu_0 = 4\pi \times 10^{-7}$ H m^{-1}, $q_e = 1.6 \times 10^{-19}$ C, $\phi = \frac{\pi}{4}$ rad for SN1, $\phi = \frac{\pi}{6}$ rad for SN2, $v_{bw} = 8 \times 10^6$ m s^{-1} into equations 18-21 yields $B_{e\_bw1} = 5.8 \times 10^{-7}$ T for SN1 and $B_{e\_bw2} = 4.0 \times 10^{-7}$ T for SN2. The average B_{e_bw} is computed using the electron density as weighting factor with

$$B_{e\_bw} = \frac{e_{dens50}}{e_{dens40} + e_{dens50}} B_{e\_bw1} + \frac{e_{dens40}}{e_{dens40} + e_{dens50}} B_{e\_bw2} = 4.7 \times 10^{-7} \text{ T} \tag{45}$$

To compute the average photon magnetic flux density B_{pavg} with equation 27, the peak photon magnetic field intensity H_{pmax} in the overlapping region sourced from a coherent EM wave emanating from the galaxy core must first be determined. For simplicity, it is assumed that the luminosity from the galaxy core is focused at the $H\alpha$ line. The power of a continuous photon stream at the $H\alpha$ frequency 4.57 x 10^{14} Hz is $P_{\gamma s} = 1.38 \times 10^{-4}$ W. With a distance to the galaxy core of approximately 35K light years, the photon EM wave intensity in the overlapping region is

Preprints (www.preprints.org) | NOT PEER-REVIEWED | Posted: 24 May 2022 doi:10.20944/preprints202005.0233.v2

$$I_{\gamma s} = \frac{P_{\gamma s}}{4\pi(35K\ LY)^2} = 1.00 \times 10^{-46}\ \text{W m}^{-2} \tag{46}$$

and

$$H_{pmax} = \sqrt{\frac{2 \cdot I_{\gamma s}}{\eta_{eff} \cdot Z_0}} = 7.29 \times 10^{-25}\ \text{A m}^{-1} \tag{47}$$

where $Z_0 = 377$ ohms is the intrinsic impedance of free space. With this value for H_{pmax}, based on equation 27 the average photon magnetic flux density is then $B_{pavg} = 5.83 \times 10^{-31}$ T.

With the values for B_{e_bw} and B_{pavg} from Section 4.4, the relative permeability in the photon/electron interaction area based on equation 44 is $\mu_r = 6.9 \times 10^{23}$. By similarity, the positive charged ions traveling with the electrons will exhibit a relative permeability of $\mu_r = -6.9 \times 10^{23}$. As discussed previously, with $\epsilon_r = 1$ the negative permeability results in an imaginary refractive index which subjects the photon to attenuation or extinction according to equation 32. With the column density of ions approximately equal to electrons, the observed extinction will be small and can be neglected here.

Continuing with the Effective Medium Theory to determine the effective permeability of the medium with respect to a photon sourced from the galactic core, equation 18 can be rearranged to yield

$$A = \frac{\pi(\frac{\lambda}{2\pi})^2 \lambda_{eff}}{4 \cdot \frac{1}{e_{dens40} + e_{dens50}}} = 9.12 \times 10^{-27} \tag{48}$$

where λ_{eff} is set to the $H\alpha$ wavelength with $\eta_{eff} \approx 1$, the term $\frac{\lambda}{2\pi}$ is the radius of the photon soliton at the $H\alpha$ wavelength and $e_{dens40} + e_{dens50}$ is the total electron density for the 2 SNBWs in the overlap region. From equation 17, the effective relative permeability μ_{r_eff} is then

$$\mu_{r\_eff} = A \cdot \mu_r + (1 - A) = 1.006 \tag{49}$$

where μ_r is based on the density weighted B_{e_bw} from equation 45. The effective refractive index η_{eff} with $\epsilon_r = 1$ is then $\eta_{eff} = \sqrt{\mu_{r\_eff}} = 1.003$. If at the shock discontinuity interface the plasma medium has an abrupt transition to free space ($\eta = 1$), the amplitude of the reflection will be consistent with the reflection coefficient Γ_r defined by

$$\Gamma_r = (\frac{\eta_{eff} - \eta}{\eta_{eff} + \eta})^2 = 2.4 \times 10^{-6}. \tag{50}$$

4.6 Plasma Permeability of Reflection

The reflected photon EM wave intensity I_{refl} can be determined from the previously calculated photon EM wave intensity from the galactic core reaching the overlapping region $I_{\gamma s}$ with the equation

$$I_{refl} = \Gamma_r \cdot I_{\gamma s}. \tag{51}$$

Then for the reflected wave, with reference to Fig. 4b, the electron magnetic flux density averaged over the period of photon/electron interaction is evaluated in two distinct regions, R1 and R2. The BW expansion velocities from SN1 and SN2 are both v_{bw}= 8,000 km s^{-1} and the BW mediums or widths are expanding at v_w= 800 km s^{-1} for both.

Preprints (www.preprints.org) | NOT PEER-REVIEWED | Posted: 24 May 2022 doi:10.20944/preprints202005.0233.v2

Region R1 consists of electrons from SN1 and SN2 which requires B_{e_bw} to be evaluated separately for each set of electrons. Starting with SN2 where the electron is angling away from the reflected photon with $\phi = \frac{\pi}{3}$, equations 40-43 are leveraged to compute B_{ebwsn2}. For SN1, where the electron is angling toward the reflected photon with $\phi = \frac{\pi}{4}$, the average electron magnetic flux density as a function of time t and position x from equation 40 is rewritten to account for the change in photon direction as

$$B_{er\_bwysn1}(t,x) = \frac{\pi}{\lambda}\int_{-\frac{\lambda}{2\pi}}^{\frac{\lambda}{2\pi}} \frac{\mu_0 q_e v_{bw}}{4\pi((x'')^2+(y')^2)} \sin(\operatorname{atan}\left(\frac{y'}{x''}\right)+\phi)dy \quad (52)$$

where $x'' = x - (\lambda_{eff} - v_{bw}\cdot t\cdot cos(\phi))$ and $y' = y - v_{bw}\cdot t\cdot \sin(\phi)$ with same constraints as previously applied. The electron magnetic flux density averaged over the period of photon/electron interaction for the reflected photon wave is then given by

$$B_{er\_bwxysn1}(t) = \frac{1}{\lambda_{eff}}\int_{c_{eff}\cdot t}^{c_{eff}\cdot t+\lambda_{eff}} B_{er\_bwysn1}(t,x)\psi'(x - c_{eff}\cdot t)dx \quad (53)$$

and

$$B_{e\_bwsn1} = \frac{c_{eff}-v_{bw}\cdot\cos(\phi)}{\lambda_{eff}}\int_0^{\frac{\lambda_{eff}}{c_{eff}-v_{bw}\cdot\cos(\phi)}} B_{er\_bwxysn1}(t)dt. \quad (54)$$

The average Region R1 B_{e_bwR1} is computed using the electron density as weighting factor with

$$B_{e\_bwR1} = \frac{e_{dens50}}{e_{dens40}+e_{dens50}} B_{e\_bwsn1} + \frac{e_{dens40}}{e_{dens40}+e_{dens50}} B_{e\_bwsn2}. \quad (55)$$

Region R2 consists of electrons from only SN2 and the previously computed B_{e_bwsn2} is applicable, such that $B_{e\_bwR2} = B_{e\_bwsn2}$. Photons from the reflection passing from Region R1 to Region R2 travel through the tapered trailing edge of the BW from SN1 which provides a gradual impedance transition with negligible reflections. Photons from the reflection exiting Region R2 travel through the leading edge of the BW from SN2 which also has a tapered profile reflecting negligible energy as it expands in the absence of ambient pressure.

Returning to the reflection from the shock interface, the peak reflected photon magnetic field intensity H_{prmax} is rewritten from equation 47 as

$$H_{prmax} = \sqrt{\frac{2\cdot I_{refl}}{\eta_{eff}\cdot Z_0}} \quad (56)$$

and

$$B_{pavg} = \frac{2\mu_0}{\lambda_{eff}}\int_0^{\frac{\lambda_{eff}}{2}} H_{prmax}\sin\left(2\pi\frac{x}{\lambda_{eff}}\right)dx. \quad (57)$$

With the values for B_{e_bwR1}, B_{e_bwR1} and B_{pavg}, the relative permeability for the reflected path in the Region R1 and the Region R2 is then computed with

$$\mu_{rR1} = \frac{B_{e\_bwR1}}{B_{pavg}} + 1 \text{ and } \mu_{rR2} = \frac{B_{e\_bwR2}}{B_{pavg}} + 1. \quad (58)$$

and the reflected effective relative permeability μ_{r_eff} is then calculated with

Preprints (www.preprints.org) | NOT PEER-REVIEWED | Posted: 24 May 2022 doi:10.20944/preprints202005.0233.v2

$$A_{R1} = \frac{\pi(\frac{\lambda}{2\pi})^2 \lambda_{eff}}{4 \cdot \frac{1}{e_{dens40}+e_{dens50}}} \quad \text{and} \quad A_{R2} = \frac{\pi(\frac{\lambda}{2\pi})^2 \lambda_{eff}}{4 \cdot \frac{1}{e_{dens40}}} \tag{59}$$

where for Region R1

$$\mu_{r\_effR1} = A_{R1} \cdot \mu_{rR1} + (1 - A_{R1}) \tag{60}$$

and for Region R2

$$\mu_{r\_effR2} = A_{R2} \cdot \mu_{rR2} + (1 - A_{R2}) \tag{61}$$

The effective refractive index for the reflected photon wave in Region R1 and Region R2 with relative permittivity $\epsilon_r = 1$ is then

$$\eta_{effR1} = \sqrt{\mu_{r\_effR1}} \text{ and } \eta_{effR2} = \sqrt{\mu_{r\_effR2}} \tag{62}$$

The effective refractive index for the reflected wave in the plasma medium is determined by sweeping the value of η_{eff} in the sequential calculations for equations 52 – 61 and 44 to converge with the value from equation 62. With the reflection coefficient Γ calculated from equation 50, the reflected refractive index converges to $\eta_{effR1} = 4.0$ for Region 1 and $\eta_{effR2} = 4.12$ for Region 2.

4.7 Redshift and Relative Magnitude of Reflection

Rearranging equation 8 to solve for the redshift z yields

$$z = \frac{v_w \cdot (\eta_{eff} - 1)}{c - v_w \cdot \eta_{eff}}. \tag{63}$$

Referencing Fig. 4b, in Region R1 the medium expansion velocity v_{wR1} along the reflected photon path is related to the medium expansion velocity of the blast shell width of SN1 v_{wSN1} by the equation

$$v_{wR1} = \frac{v_{wSN1}}{\cos(\phi)}, \tag{64}$$

where with v_{wSN1}=800 km s^{-1} and $\phi = \frac{\pi}{4}$ yields v_{wR1}= 1,131 km s^{-1}. In Region R2 the medium expansion velocity v_{wR2} along the reflected photon path is computed based on the sum of trailing edge velocity of the SN1 BW v_{bwSN1T} and the leading edge velocity of the SN2 BW v_{bwSN2L} with equation

$$v_{wR2} = \frac{v_{bwSN1T}}{\cos(\phi_1)} + \frac{v_{bwSN2L}}{\cos(\phi_2)}, \tag{65}$$

where with v_{bwSN1T} = 7,200 km s^{-1}, v_{bwSN2L} = 8,000 km s^{-1}, $\phi_1 = \frac{\pi}{4}$ and $\phi_2 = \frac{\pi}{3}$ yields v_{wR2} = 26,180 km s^{-1}. As defined by equations 64 and 65, SNBW geometries with larger angles for ϕ can significantly increase v_w which in turn drives up z for a given effective refractive index η_{eff}.

Substituting the values for v_w and η_{eff} computed for Regions R1 and R2 into equation 63 results in a redshift of $z_{R1} = 0.01$ for Region R1 and $z_{R2} = 0.44$ for Region R2. The sequential redshifts combine to yield a net redshift of $z = 0.46$ for the reflected photon wave relative to the host galaxy. Since the variables in equation 63 are not set near a pole or zero, the associated redshift is largely achromatic.

The magnitude difference between the reflection and the galactic core of Fig. 4b is determined based on viewing the galaxy edge-on, as the reflection travels parallel to the galactic plane. Approximating the

Preprints (www.preprints.org) | NOT PEER-REVIEWED | Posted: 24 May 2022 doi:10.20944/preprints202005.0233.v2

edge-on galactic core light as concentrated within area A_{gc} defined as a rectangle 26k LY across and 1k LY thick and assuming the star distribution is uniform such that the average face-on surface intensity

$$I_{face} = \frac{L_{core}}{\pi(R_{core})^2}, \tag{66}$$

and with dust and gas from the ISM mixed with the star field, if the face-on intensity is maintained from the edge, then the edge-on luminosity can be expressed

$$L_{edge} = I_{face} \cdot A_{gc} = 4.71 \times 10^{35} \text{ W}. \tag{67}$$

Referring to Fig. 4c, the arc reflection of 30 degrees with respect to the focal plane as shown has a spherical surface formed from a SNe 50k LY away and the arc reflection has an approximate surface area of $A_{aseg} = 5.8 \times 10^{39}$ m^2. The reflection is sourced with light from the galactic core which passes through a central focal area spaced 25k LY away in the direction of the galaxy center. The central focal area can be approximated by the intersection formed by a projection of the reflection surface area to a point 50k LY below the galaxy center with a focal plane positioned 25K LY below the reflection and parallel to the galactic core. The intersection traces out a focal plane surface area $A_{fp} = \frac{A_{aseg}}{\left(\frac{50}{25}\right)^2} = 1.46 \times 10^{39}$. The focal plane surface area is 10K LY above the galactic core and the projection continues onto the galactic core to trace out a central source region with surface area of $A_{gcfa} = \frac{A_{aseg}}{\left(\frac{50}{15}\right)^2} = 5.26 \times 10^{38}$. The luminosity of the galactic core region sourcing the reflection can be approximated by $L_{gcsa} = I_{face} \cdot A_{gcfa} = 1.06 \times 10^{35}$. Then the estimated total luminosity from the source area incident on the arc segment can be computed by the amount of galactic core source area luminosity passing through the focal surface area A_{fp} at $H = 10$k LY above the galactic core as $L_{ainc} = L_{gcsa} \cdot \frac{A_{fp}}{4\pi(H)^2} = 1.38 \times 10^{33}$.

The reflected luminosity of the arc segment L_{arefl} can then be expressed

$$L_{arefl} = L_{ainc} \cdot \Gamma_r \cdot G_{sph} = 3.31 \times 10^{29}, \tag{68}$$

where Γ_r is from equation 49 and the term G_{sph} factors in 20dB gain which is typical for a spherical reflector. If the arc spans 60 degrees, the luminosity L_{arefl} will increase by an approximate factor of 2.

The observed magnitude difference between the reflection from the 60 degree arc and the edge-on galactic core is then

$$\Delta m = -2.5 log_{10}\left(\frac{2 \times L_{arefl}}{L_{edge}}\right) = +14.6. \tag{69}$$

This value for Δm is in the range of the magnitude difference between the moon and the sun.

5. Einstein Cross Structures

The Hubble Space Telescope has captured numerous images where a quadruple light source structure is formed around a central galaxy, referred to as an Einstein Cross [59]. These Einstein Cross structures are formed from 4 intersecting CG-BWs where the quadruple image is comprised of redshifted reflected light from the central galaxy. With the CG-BWs having expanded to radii in the range of 50k LY or more, the

Preprints (www.preprints.org) | NOT PEER-REVIEWED | Posted: 24 May 2022 doi:10.20944/preprints202005.0233.v2

time since the respective SNs exploded would be >1.5 million years. As a result, the underlying SNes may have been separated in time by up to 10k years or more.

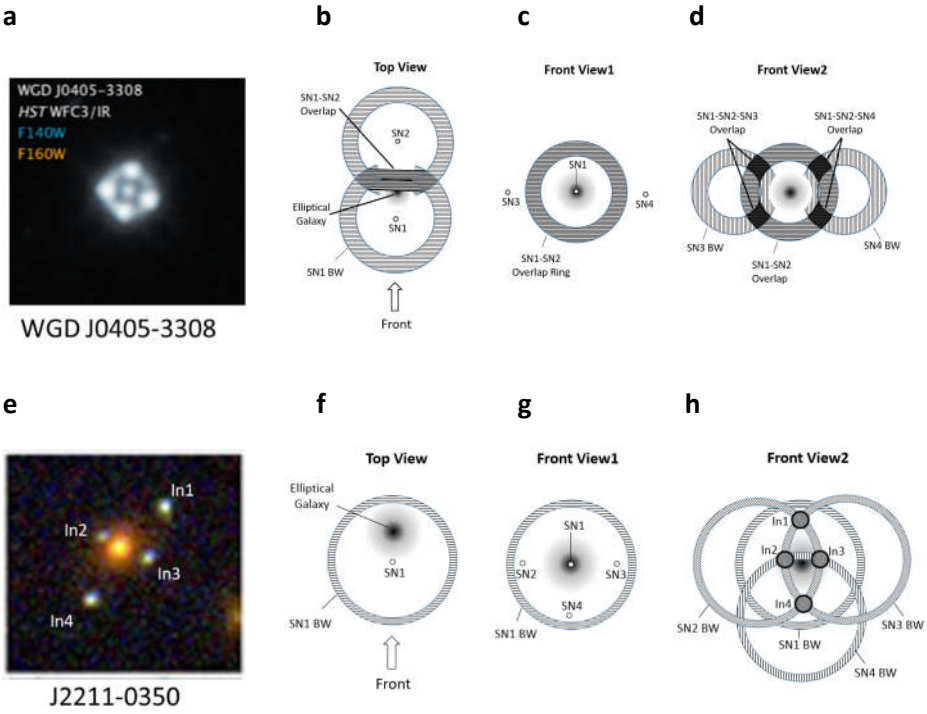

Fig. 5. Einstein Cross images and underlying CG-BWs. (a) Image of Einstein Cross WGD J0405-3308. **(b&c)** Top and front view of intersection ring formed from SN1 and SN2. **(d)** Triple intersections of blast waves SN1-SN4 forming the Einstein Cross pattern in dark grey. **(e)** Image J2211-0350 with Einstein Cross. **(f&g)** Top and front view of SN1 blast wave. **(h)** Triple intersections of blast waves forming the Einstein Cross pattern points In1-In4.

Fig 5a is a Hubble Space Telescope image of Einstein Cross WGD-J0405-3308 which is considered the front view orientation in the following descriptions. Fig. 5b is a top view of the structure with two of the four SN blast waves shown with a horizontal hash pattern positioned in front of and behind the central elliptical galaxy. The SNs are distanced from the central galaxy such that only an approximate 30 degree sector of the blast waves are substantially absorbed and blocked by the galaxy. The overlap of the SN1 and SN2 blast waves form a ring which can be seen in the front view of Fig. 5c, along with the positions of SN3 and SN4. In Fig. 5d, the blast waves from SN3 and SN4 are shown in vertical crosshatch. The intersection of the ring from SN1 and SN2 with the spherical blast waves from SN3 and SN4 form 4 shocked overlapping regions as shown with triple the plasma density of a single blast wave, which creates the bright reflections at the Einstein Cross points. Note that the rectangular cross section of the dark shaded triple overlap regions in Fig. 5d are partially visible in the Fig. 5a image. Fig. 5e is a Hubble Space Telescope image of an Einstein Cross configuration found in galaxy cluster J2211-0350 [60]. Fig. 5f is a top view of the structure which includes the central elliptical galaxy and the position of SN1 and its associated blast wave. Fig. 5g is a front view which includes the positions of SN2, SN3 and SN4 around the galaxy. In Fig. 5h, the blast waves of SN2, SN3 and SN4 are added. The blast waves from SN2 and SN3 intersect to form an overlap ring. This ring intersects the spherical blast wave from SN1 at the far side of the elliptical galaxy at intersection points In1 and In4. Similarly, the blast waves from SN2 and SN4 and the blast waves from SN3 and SN4 form rings which intersect with SN1's blast wave at points In3 and In2, respectively. The intersections In1 to In4 are each comprised of 3 blast waves with triple the

Preprints (www.preprints.org) | NOT PEER-REVIEWED | Posted: 24 May 2022 doi:10.20944/preprints202005.0233.v2

plasma density of a single blast wave, driving bright reflections from the outer shocked surface of SN1's blast wave which forms the Einstein Cross points.

Galaxy clusters are known to host multiple gravitational lensing events. In some cases, the summation of the cluster mass creates a gravitational field which bends the light of a distant galaxy to create a large cluster arc, such as the "Sunburst Arc" observed with the Hubble Telescope [61]. Analysis of large circular arcs formed near galaxy clusters indicate the Einstein radii determined by the cluster mass density versus the area enclosed by the arc can differ by 10-30% [62]. Since tidal stripping in galaxy clusters can drive large populations of stars into the IGM, it is feasible that the associated freely expanding blast waves can reach the radii of the observed cluster arcs and overlapping blast waves can produce gravitational lens structures equivalent to the "Sunburst Arc".

Measurements of gravitational microlensing of near-field objects, such as a foreground star crossing in front of a background star, experience similar uncertainties as present imaging limitations do not allow accurate resolution of the lens from the source at the time of the event [63].

Einstein Cross structures have been successfully replicated with gravitational lensing models by deploying complex arrangements of dark matter substructures with varying density [64]. Observational evidence indicates that these dark matter substructures arrange themselves to only produce Einstein Crosses. In Hubble Telescope images of large galaxy clusters containing around a thousand galaxies, strong lensing of numerous background galaxies has been detected. Underlying mass models, including dark matter substructures, have been constructed by applying parametric lens inversion tools to the identified lensed galaxies in the clusters. Simulations using these mass structures show the number of predicted galaxy-galaxy strong lensing events within the standard cosmological model are an order of magnitude lower than the number of observed events [65]. As imaging technologies improve, the body of observational evidence exhibiting unexplained inconsistencies with the gravitational lens model continues to accumulate.

6. The Hubble Constant

Application of the CG-BW electrodynamic properties to incoming extragalactic light fields can emulate characteristics of the Hubble Law

$$H_0 = {}^{v_r}/_{d} \tag{70}$$

where H_0 is the Hubble constant, v_r is the recession velocity and d is the distance to an observed extragalactic object. Ongoing measurements of the Hubble constant using different distance estimation techniques have not been able to converge on a single value [66,67]. The convergence problem is related in part to the difficulty in establishing an accurate distance to an observed object over large cosmological scales. Numerous methods are used for distance estimation including Type Ia SN, which relies on known SN luminosity, the Tully-Fisher Relation (TFR), which for late-type galaxies relies on a measurement of the galaxy's rotational velocity to infer the intrinsic luminosity, and the Cepheid star which relies on measurement of the Cepheid period to estimate the star's luminosity [68]. For each method, the objects inferred luminosity is used in conjunction with the observed luminosity to estimate the distance. Of these techniques, only the measurement of the Cepheid period is subject to change due to redshift. In this case, the increase in Cepheid period from recession due to an expanding universe would appear identical had the recession occurred while an intervening media with refractive index >1 was expanding. Hence the referenced measurement techniques are expected to be independent of the mechanism inducing the recession velocity.

Preprints (www.preprints.org) | NOT PEER-REVIEWED | Posted: 24 May 2022 doi:10.20944/preprints202005.0233.v2

The recession velocity v_r can be expressed

$$v_r = c \cdot z. \tag{71}$$

Equation 71 can be rewritten in terms of the SN blast wave parameters derived in previous sections. Substituting equation 63

$$z = \frac{v_w \cdot (\eta_{eff} - 1)}{c - v_w \cdot \eta_{eff}} \tag{63}$$

with expanded terms from equations 9, 17 and 44 and rewriting equation 71 as a function of distance d in Mpc yields

$$v_r(d) = \frac{c}{1000} \cdot \frac{v_w \cdot \left(\left(\left(A \cdot \left(\frac{B_{e\_bw}}{B_{pavg}(d)} + 1 \right) + (1 - A) \right) + 1 \right)^{\frac{1}{2}} - 1 \right)}{c - v_w \cdot \left(\left(A \cdot \left(\frac{B_{e\_bw}}{B_{pavg}(d)} + 1 \right) + (1 - A) \right) + 1 \right)^{\frac{1}{2}}} \text{ km s}^{-1} \tag{72}$$

where

$$B_{pavg}(d) = \frac{2 \cdot \mu_0}{\lambda} \cdot \int_0^{\frac{\lambda}{2}} \left(\frac{2 \cdot I_{YS} \cdot (1 - a_{dust})^d}{Z_0 \cdot 4 \cdot \pi \cdot (d \cdot 3.26 \cdot 10^6 \cdot LY)^2} \right)^{\frac{1}{2}} \cdot sin\left(2\pi \frac{x}{\lambda}\right) dx \tag{73}$$

and a_{dust} is the average factor of photon soliton intensity lost per Mpc due to intergalactic dust attenuation.

The plots of Fig. 6 have been generated by loading equations 72 and 73 with exemplary parameters $v_w =$ 800 km s^{-1}, $A = 9.5 \times 10^{-27}$ and $B_{e\_bw} = 6.8 \times 10^{-7}$ T to demonstrate the characteristics of the plasma-induce redshift over a wide range of distances.

a **b**

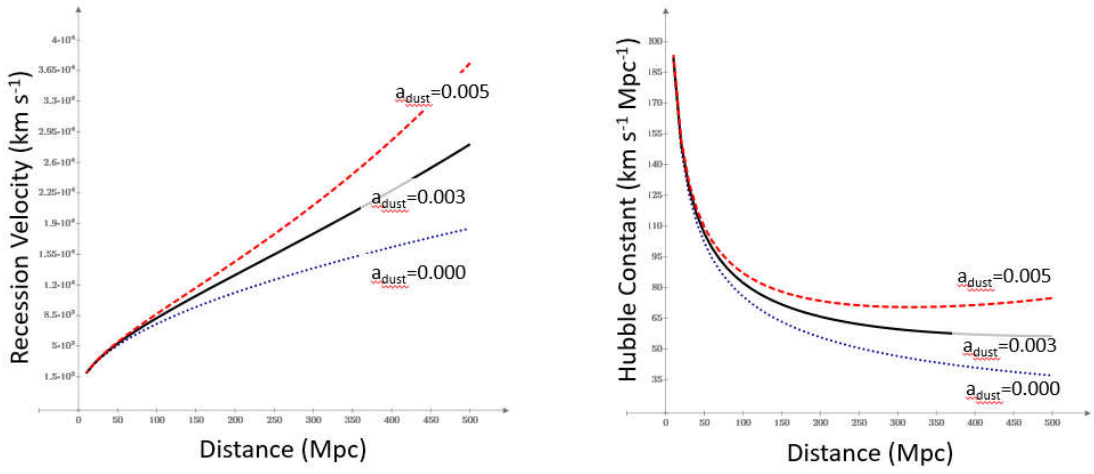

Fig. 6. Plots of Plasma-Based Equations for Recession Velocity and Hubble Constant. **(a)** Recession Velocity vs. Distance plots for multiple dust attenuation factors. **(b)** Hubble Constant vs. Distance plots for multiple dust attenuation factors.

Preprints (www.preprints.org) | NOT PEER-REVIEWED | Posted: 24 May 2022 doi:10.20944/preprints202005.0233.v2

Fig. 6a shows a plot of the recession velocity vs. distance and Fig. 6b the Hubble Constant vs. distance defined by

$$H_0(d) = {}^{v_r(d)}/_{d} \quad (74)$$

with the intergalactic dust attenuation factor set to 0.000, 0.003 and 0.005. The impact of intergalactic dust can be seen where a_{dust} can be adjusted along with other parameters to closely match Hubble Constant H_0 estimates for both early time and late time observation campaigns. Equations 72 and 73 do not factor in secondary effects which are expected to moderate the slope at distances below 50 Mpc. Recession velocity observations in this region are noisy and can be impacted by multiple low level contributing factors, including but not limited to negative relative source velocity bias, blueshifts from active compression of plasma at the source or from the velocity of plasma inflows at the source, where the latter has an asymmetrically dominant influence on outgoing light fields. Without additional factors to account for low velocity bias, parameter optimization could be leveraged to accurately align the plots with existing observation campaigns beyond 50 Mpc.

7. Summary

Aside from reflections off shock discontinuities, direct evidence of freely expanding CG-BWs is predictably difficult to find in the large body of observational data on the Milky Way due to 1) the low rate of occurrence reduces early phase detections, 2) the plasmas rapidly cool, are optically thin and non-emissive, 3) the propagation medium is too thin to generate a detectable radio emission and 4) the plasma density is too low for detection by absorption spectroscopy. The extensive observational data on galactic halos and CGMs do not rule out CG-BWs and has been shown to provide evidence lending support to their existence.

The analysis presented demonstrates CG-BWs exhibit paramagnetic properties which significantly influence the propagation of EM waves. The dominant mechanism driving up the plasma permeability is the particle velocity imparted by the SNe, where during the period an electron crosses the path of an interacting photon soliton it introduces an asymmetric magnetic field inside the interaction region which aligns in-phase with the photon magnetic field. When SN blast waves intersect, the discontinuity in permeability across the shocked surface reflects light from the host galaxy exposing the overlapping blast wave sections which naturally form rings, arcs or Einstein Crosses. The permeability of the expanding blast wave shells is shown to redshift the reflected light consistent with the measured light spectrum of these structures observed in the universe. Einstein Cross observations provide strong direct evidence supporting the analysis as these configurations are naturally formed by overlapping SN blast waves.

Equations for the plasma permeability rely on a coherent photon soliton wave interacting with a high-velocity low-density plasma spread out over thousands of light years. As the computed plasma effective index of refraction is dependent on the photon soliton amplitude but not the number of photons, the resultant redshift is governed by factors impacting the path loss from the source, such as attenuation due to distance and dust. This implies objects with wide-ranging intensity that are at the same distance may be observed at the same redshift. It is possible future models could be developed to show high velocity plasma interactions can reproduce other cosmic phenomena such as the Lyman-Alpha Forest and odd radio circles. Theoretically, the equations derived for the Hubble constant could be leveraged in connection with additional observations to build a model of the CG-BW environment around the Milky Way.

Conflicts of Interest: The author declares no conflict of interest.

References:

[1] U. S. Inan, M. Golkowski, "Introduction to waves in plasmas" in *Principles of Plasma Physics for Engineers and Scientists* (Cambridge Univ. Press, 2011).
[2] J. Nilsen, W. R. Johnson, *Analysing the dramatic impact of the bound electron contribution to the index of refraction in plasmas*, (2004).
[3] D. Branch, J. C. Wheeler, *Supernova Explosions* (Springer, 2017).
[4] E. O. Ofek, I. Arcavi, D. Tal, M. Sullivan, A. Gal-Yam, S. R. Kulkarni, P. E. Nugent, S. Ben-Ami, D. Bersier, Y. Cao, S. B. Cenko, A. De Cia, A. V. Filippenko, C. Fransson, M. M. Kasliwal, R. Laher, J. Surface, R. Quimby, O. Yaron, Interaction-powered supernovae: rise-time vs. peak-luminosity correlation and the shock-breakout velocity. *Ap. J.* **788**, 154 (2014).
[5] D. Branch, M. Livio, L. R. Yungelson, F. R. Boffi, E. Baron, In search of the progenitors of Type Ia supernovae. *Pub. A.S. Pac.* **107**, 1019-1029 (1995).
[6] A. V. Filippenko, Optical spectra of supernovae. *A.R. A.&A.* **35**, 309-55 (1997).
[7] W. Hillebrandt, J. C. Niemeyer, Type Ia supernova explosion models. *A.R. A.&A.* **38**, 191-230 (2000).
[8] P. Hoflick, A. Khokhlov, Explosion models for Type Ia supernovae: a comparison with observed light curves, distances, H_0, and q_0. *Ap. J.* **457**, 500-528 (1996).
[9] S. Haid, S. Walch, T. Naab, D. Seifried, J. Mackey, A. Gatto, Supernova-blast waves in wind-blown bubbles, turbulent, and power-law ambient media. *MNRAS* **460**, 2962-2978 (2016).
[10] F. G. Freidlander, The diffraction of sound pulses I. Diffraction by a semi-infinite plane. *Proc. Roy. Soc. Lond. A* **186**, 322-344 (1946).
[11] D. A. Gurnett, A. Bhattacharjee, "Discontinuities and Shock Waves" in *Introduction to Plasma Physics* (Cambridge Univ. Press, 2017).
[12] B. W. Keller, J. Wadsley, H. M. P. Couchman, Cosmological galaxy evolution with superbubble feedback – I. Realistic galaxies with moderate feedback. *MNRAS* **453**, 3499-3509 (2015).
[13] V. Springel, L. Hernquist, Cosmological smoothed particle hydrodynamics simulations: a hybrid multiphase model for star formation. *MNRAS* **339**, 289-311 (2003).
[14] G. Stinson, A. Seth, N. Katz, J. Wadsley, F. Governato, T. Quinn, Star formation and feedback in smoothed particle hydrodynamic simulations – I. Isolated galaxies. *MNRAS* **373**, 1074-1090 (2006).
[15] M. Li, G. L. Bryan, J. P. Ostriker, Quantifying supernovae-driven multiphase galactic outflows. *Ap. J.* **841**, 101-116 (2017).
[16] C. Heiles, Clustered supernovae versus the gaseous disk and halo. *Ap. J.* **354**, 483-491 (1990).
[17] C-G. Kim, E. C. Ostriker, R. Raileanu, Superbubbles in the multiphase ISM and the loading of galactic winds. *Ap. J.* **834**, 25 (2017).
[18] A Camps-Farina, J. Zaragoza-Cardiel, J. E. Beckman, J. Font, P. F. Valazquez, A. Rodriguez, M. Rosado, Physical properties of superbubbles in the Antennae galaxies. *MNRAS* **468**, 4134-4142 (2017).
[19] B. T. Draine, *Physics of the Interstellar and Intergalactic Medium* (Princeton University Press, 2011).
[20] G. Courtes, H. Petit, J.-P. Sivan, S. Dodonov, M. Petit, Hα survey of M33 with the six-meter telescope: Morphology of the general diffuse emission, evidence for a chaotic medium of bubbles and filaments. *A.&A.* **174**, 28-56 (1987).
[21] S. Diel, T. S. Statler, The hot interstellar medium of normal elliptical galaxies. II. Morphological evidence for active galactic nucleus feedback. *Ap. J.* **680**, 897-910 (2008).
[22] S. Malhotra, D. Hollenbach, G. Helou, N. Silbermann, E. Valjavec, R. H. Rubin, D. Dale, D. Hunter, N. Lu, S. Lord, H. Dinerstein, H. Thronson, Probing the interstellar medium in early-type galaxies with Infrared Space Observatory observations. *Ap. J.* **543**, 634-643 (2000).
[23] M. T. Sargent, E. Daddi, F. Bournaud, M. Onodera, C. Feruglio, M. Martig, R. Gobat, H. Dannerbauer, E. Schinnerer, A direct constraint on the gas content of a massive, passively evolving elliptical galaxy at z = 1.43. *Ap. J. Lett.* **806**, L20 (2015).
[24] G. A. Welch, L. J. Sage, The interstellar medium of M32. *Ap. J.* **557**, 671-680 (2000).
[25] J. Maza, S. van den Bergh, Statistics of extragalactic supernova. *Ap. J.* **204**, 519-529 (1976).
[26] D. J. Patnaude, C. Badenes, S. Park, J. M. Laming, The origin of Kepler's supernova remnant. *Ap. J.* **756**, 6 (2012).
[27] I. J. Danziger, W. M. Goss, The distance of Kepler's supernova remnant. *MNRAS* **190**, 47-49 (1980).
[28] S. van den Bergh, A. P. Marscher, Y. Terzian, An optical atlas of galactic supernova remnants. *Ap. J. S.S.* **26**, 19-36 (1973).
[29] S. P. Reynolds, K. J. Borkowski, U. Hwang, J. P. Hughes, C. Badenes, J. M. Laming, J. M. Blondin, A deep Chandra observation of Kepler's supernova remnant: A Type Ia event with circumstellar interaction. *Ap. J.* **668**, L135-L138 (2007).
[30] C. F. McKee, J. P. Ostriker, A theory of the interstellar medium: Three components regulated by supernova explosions in an inhomogeneous substrate. *Ap. J.* **218**, 148-169 (1977).
[31] S. M. Adams, C. S. Kochanek, J. F. Beacom, M. R. Vagins, K. Z. Stanek, Observing the next galactic supernova. *Ap. J.* **778**, 164-179 (2013).
[32] K. L. Adelberger, C. C. Steidel, A. E. Shapley, M. Pettini, Galaxies and intergalactic matter at redshift z ~ 3: Overview. *Ap. J.* **584**, 45-75 (2003).
[33] A. Aguirre, L. Hernquist, J. Schaye, D. H. Weinberg, N. Katz, J. Gardner, Metal enrichment of the intergalactic medium at z = 3 by galactic winds. *Ap. J.* **560**, 599-605 (2001).
[34] J. M. Shull, Where do galaxies end?, *Ap. J.* **784**, 142 (2014).
[35] J. X. Prochaska, J. K. Werk, G. Worseck, T. M. Tripp, J. Tumlinson, J. N. Burchett, A. J. Fox, M. Fumagalli, N. Lehner, M. S. Peeples, N. Tejos, The COS-Halos Survey: Metallicities in the low-redshift circumgalactic medium. *Ap. J.* **837**, 169 (2017).
[36] T. M. Heckman, Starburst-driven galactic winds. *Rev. Mex. AA* **17**, 47-55 (2003).
[37] M. S. Peeples, F. Shankar, Constraints on star formation driven galaxy winds from the mass-metallicity relation at z = 0. *MNRAS* **417**, 2962-2981 (2011).

[38] D. K. Strickland, T. M. Heckman, Supernova feedback efficiency and mass loading in the starburst and galactic superwind exemplar M82. *Ap. J.* **697**, 2030-2056 (2009).
[39] B. D. Savage, K. R. Sembach,B. P. Wakker, P. Richter, M. Meade, E. B. Jenkins, J. M. Shull, H. W. Moos, G. Sonneborn, Distribution and kinematics of O VI in the galactic halo. *Ap. J.* **146**, 125-164 (2003).
[40] J. Roman-Duval, M. Heyer, C. M. Brunt, P. Clark, R. Klessen, R. Shetty, Distribution and mass of diffuse and dense CO gas in the Milky Way. *Ap. J.* **818**, 144 (2016).
[41] R. Ganguly, K. Sembach, T.M. Tripp, B. D. Savage, Highly ionized gas in the galactic halo and the high-velocity clouds toward PG 1116+215. *Ap. J.S.S.* **157**, 251-278 (2005).
[42] K. R. Sembach, B. P. Wakker, B. D. Savage, P. Richter, M. Meade, J. M. Shull, E. B. Jenkins, G. Sonneborn, H. W. Moos, Highly ionized high-velocity gas in the vicinity of the galaxy. *Ap. J.S.S.* **146**, 165-208 (2003).
[43] J. A. Gritton, R. L. Shelton, K. Kwak, Mixing between high velocity clouds and the galactic halo. *Ap. J.* **795**, 99 (2014).
[44] E. Shulman, J. N. Bregman, M. S. Roberts, An H I survey of high-velocity clouds in nearby disk galaxies. *Ap. J.* **423**, 180-189 (1994).
[45] F. J. Lockman, The H I halo in the inner galaxy. *Ap. J.* **283**, 90-97 (1984).
[46] E. Hummel, R. Beck, R.-J. Dettmar, An Effelsberg/VLA radio continuum survey of an optically selected sample of edge-on spiral galaxies. *A&A S.S.* **87**, 309-317 (1991).
[47] C. Heiles, H I shells and supershells. *Ap. J.* **229**, 533-544 (1979).
[48] C. Heiles, H I shells, supershells, shell-like objects, and "worms". *Ap. J. S.S.* **55**, 585-595 (1984).
[49] R. W. Klopfenstein, A transmission line taper of improved design. *Proc. I.R.E.* **1**, 31-35 (1956).
[50] B. T. Draine, C. F. McKee, Theory of interstellar shocks. *A.R. A.&A.* **31**, 373-432 (1993).
[51] E. O. Ofek, H.-W. Rix, D. Maoz, The redshift distribution of gravitational lenses revisited: constraints on galaxy mass evolution, *MNRAS* **343,** 639–652 (2003).
[52] M Fukugita, T. Futamase, M. Kasai, E. L. Turner, Statistical properties of gravitational lenses with a nonzero cosmological constant. *Ap. J.* **393**, 3-21 (1992).
[53] W. H. Hayt, "The Uniform Plane Wave" in *Engineering Electromagnetics* (McGraw-Hill, 1974).
[54] U. S. Inan, M. Golkowski, "Collisions and plasma conductivity" in *Principles of Plasma Physics for Engineers and Scientists* (Cambridge Univ. Press, 2011).
[55] T. J. Cui, W. X. Tang, X. M. Yang, Z. L. Mei, W. X. Jiang, "Artificial Particles" in *Metamaterials* (CRC Press, 2016).
[56] C. Roychoudhuri, A. F. Kracklauer, K. Creath, "The Bohr Model of the Photon" in *The Nature of Light* (CRC Press, 2008).
[57] C. Flynn, J. Holmberg, L. Portinari, B. Fuchs, H. JahreiB, On the mass-to-light ratio of the local galactic disc and the optical luminosity of the galaxy. *MNRAS* **372**, 1149-1160 (2006).
[58] J. Weingartner, B. T. Draine, Dust grain-size distributions and extinction in the Milky Way, Large Magellanic Cloud, and Small Magellanic Cloud. *Ap. J.* **548**, 296-309 (2001).
[59] A. M. Nierenberg, D. Gilman, T. Treu, G. Brammer, S. Birrer, L. Moustakas, A. Agnello, T. Anguita, C. D. Fassnacht, V. Motta, A. H. G. Peter, D. Sluse, Double dark matter vision: twice the number of compact-source lenses with narrow-line lensing and the WFC3 grism. *MNRAS* **492**, 5314-5335 (2019).
[60] D. Bettoni, R. Falomo, R. Scarpa, M. Nagrello, A. Omizzolo, R. L. M. Corradi, D. Raverte, B. Vulcani, A new Einstein Cross gravitational lens of a Lyman-break galaxy. *Ap. J. Lett.* **873**, L14 (2019).
[61] T. E. Rivera-Thorsen, H. Dahle, J. Chisholm, M. K. Florian, M. Gronke, J. R. Rigby, M. D. Gladders, G. Mahler, K. Sharon, M. Bayliss, Gravitational lensing reveals ionizing ultraviolet photons escaping from a distant galaxy. *Sci.* **366**, 738-741 (2019).
[62] E. Puchwein, S. Hilbert, Cluster strong lensing in the Millennium simulation: the effect of galaxies and structures along the line-of-sight. *MNRAS* **398**, 1298-1308 (2009).
[63] C. B. Henderson, H. Park, T. Sumi, A. Udalski, A. Gould, Y. Tsapras, C. Han, B. S. Gaudi, V. Bozza, F. Abe, D. P. Bennett, I. A. Bond, C. S. Botzler, M. Freeman, A. Fukui, D. Fukunaga, Y. Itow, N. Koshimoto, C. H. Ling, K. Masuda, Y. Matsubara, Y. Muraki, S. Namba, K. Ohnishi, N. J. Rattenbury, T. Saito, D. J. Sullivan, D. Suzuki, W. L. Sweatman, P. J. Tristram, N. Tsurumi, K. Wada, N. Yamai, P. C. M. Yock, A. Yonehara, M. K. Szymanski, M. Kubiak, G. Pietrzynski, I. Soszynski, J. Snowron, S. Kozlowski, R. Poleski, K. Ulaczyk, L. Wyrzykowski, P. Pietrukowicz, L. A. Almeida, M. Bos, J.-Y. Choi, G. W. Christie, D. L. Depoy, S. Dong, M. Freidmann, K.-H. Hwang, F. Jablonski, Y. K. Jung, S. Kaspi, C.-U. Lee, D. Maoz, J. McCormick, D. Moorehouse, T. Natusch, H. Ngan, R. W. Pogge, I.-G. Shin, Y. Shvartzvald, T.-G. Tan, G. Thornley, J. C. Yee, A. Allan, D. M. Bramich, P. Browne, M. Dominik, K. Horne, M. Hundertmark, R. Figuera Jaimes, N. Kains, C. Snodgrass, I. A. Steele, R. A. Street, Candidate gravitational microlensing events for future direct lens imaging. *Ap. J.* **794**, 71 (2014).
[64] J. Brehmer, S. Mishra-Sharma, J. Hermans, G. Louppe, K Cranmer, Mining for dark matter substructure: inferring subhalo population properties from strong lenses with machine learning, *Ap. J.* **886**, 49-55 (2019).
[65] M. Meneghetti, G. Davoli, P. Bergamini, P. Rosati, P. Natarajan, C. Giocoli, G. B. Caminha, R. B. Metcalf, E. Rasia, S. Borgani, F. Calura, C. Grillo, A. Mercurio, E. Vanzella, An excess of small-scale gravitational lenses observed in galaxy clusters. *Sci.* **369**, 1347-1351 (2020).
[66] W. L. Freedman, B. F. Madore, B. K. Gibson, L. Ferrarese, D. D. Kelson, S. Sakai, J. R. Mould, R. C. Kennicutt, Jr., H. C. Ford, J. A. Graham, J. P. Huchra, S. M. G. Hughes, G. D. Illingworth, L. M. Macri, P. B. Stetson, Final results from the Hubble Space Telescope key project to measure the Hubble constant. *Ap. J.* **553**, 47-72 (2001).
[67] X-P. Wu, Z. Deng, Z. Zou, L.-Z. Fang, B. Qin, On the measurement of the Hubble Constant in a local low-density universe. *Ap. J.* **448**, L65-L68 (1995).
[68] W. L. Freedman, B. F. Madore, B. K. Gibson, L. Ferrarese, D. D. Kelson, S. Sakai, J. R. Mould, R. C. Kennicutt, H. C. Ford, J. A. Graham, J. P. Huchra, S. M. G. Hughes, G. D. Illingworth, L. M. Macri, P. B. Stetson, Final results from the Hubble Space Telescope Key Project to measure the Hubble Constant. *Ap. J.* **553**, 47-72 (2001).